Editor Initial Decision: Reconsider after minor revisions (Editor review) (16 Oct 2015) by William Lahoz

Comments to the Author:
Please address the comments in the attached file. I would be grateful if you could provide two versions of the revised paper, one with and one without tracking.

We thank the Editor for this careful review of our manuscript. We have revised our manuscript following all but two of his suggestions. The explanations why we did not follow these two suggestions are explained below. Please, find the marked-up version of the manuscript at the end of this document.

Page 23, Line 587: I suggest you spell out here the reason.

We think that we cannot detail these different reasons once again since explaining them requires one long paragraph in Section 3.1.1 and they cannot really be summarized in one sentence. We now refer to Section 3.1.1 in the text:

"In general, the differences of the inversion skill between July and December look consistent with what has been analyzed at the pixel scale. In particular the uncertainty reduction is higher in July for western countries but higher in December for eastern countries for the same reasons as that given when analyzing the same behavior at the pixel scale (see Sect. 3.1.1)."

Page 34, Line 884 : Section 4 is very long. I suggest you split it into a discussion section and a conclusions section, with the conclusions section shorter and summarizing the results from the study

The Editor already raised such a suggestion during the review before the paper was accepted in ACPD. We still have the same point of view regarding it: "The section cannot be easily split because its role is to carefully discuss all the results of the study: it is long because we do not want to leave the reader with simplistic messages and prefer to qualify each statement. Of course we can add a short conclusion, but we also do not want to repeat the abstract and be too much redundant with this section. Therefore at this stage, we prefer to leave this part as it is." Our feeling is that the present logical structure of the last section works well and that by extracting some information to build a conclusion section would break it. On the other hand, duplicating some of the ideas of this section to create a new conclusion section would yield some redundancies with the abstract.

However, if the Editor thinks that it is a critical issue, we are ready to try to adapt our text to this suggestion.

Note that we also decided to define that, in our text, summer and winter seasons systematically relate to seasons in the Northern hemisphere early in the text instead of using the notation northern summer/winter throughout the text: *"We consider the results for July and December to be representative for the summer and winter seasons (using the name of the seasons for the Northern Hemisphere hereafter),…"*.

On the potential of ICOS atmospheric CO_2 measurement network for the estimation of the biogenic CO_2 budget of Europe

N. Kadygrov[1], G. Broquet[1], F. Chevallier[1], L. Rivier[1], C. Gerbig[2] and P. Ciais[1]

[1] Laboratoire des Sciences du Climat et de l'Environnement, CEA-CNRS-UVSQ, 91191, Gif sur Yvette Cedex, France

[2] Max Planck Institute for Biogeochemistry, Jena, Germany

Correspondence to: N. Kadygrov (kadygrov@gmail.com)

Abstract

We present a performance assessment of the European Integrated Carbon Observing System (ICOS) atmospheric network for constraining European biogenic CO_2 fluxes (hereafter Net Ecosystem Exchange, NEE). The performance of the network is assessed in terms of uncertainty in the fluxes using a state-of-the-art mesoscale variational atmospheric inversion system assimilating hourly averages of atmospheric data to solve for NEE at 6 hour and 0.5º resolution. The performance of the ICOS atmospheric network is also assessed in terms of uncertainty reduction compared to typical uncertainties in the flux estimates from ecosystem models that are used as prior information by the inversion. The uncertainty in inverted fluxes is computed for two typical periods representative of northern summer and winter conditions in July and in December 2007, respectively. These computations are based on a Observing System Simulation Experiment (OSSE) framework. We analyze the uncertainty in two-week mean NEE as a function of the spatial scale, with a focus on the model native grid scale (0.5°), the country scale and the European scale (including western Russia and Turkey). Several network configurations, going from 23 to 66 sites, and different configurations of the prior uncertainties and atmospheric model transport errors are tested in order to assess and compare the improvements that can be expected in the future from the extension of the network, from improved prior information or transport models. Assimilating data from 23 sites (a network comparable to present day capability) with errors estimated from the present prior information and transport models, the uncertainty reduction on two-week mean NEE should range between 20% and 50% for 0.5° resolution grid cells in the best sampled area encompassing eastern France and western Germany. At the European scale, the prior uncertainty in two-week mean NEE is reduced by 50% (66%), down to ~ 43 TgCmonth^{-1} (26 TgCmonth^{-1}) in July (December). Using a larger network of 66 stations, the prior uncertainty of NEE is reduced by the inversion by 64% (down to ~33 TgC month^{-1}) in July and by 79% (down to ~15 TgC month^{-1}) in December. When the results are integrated over the well-observed western European domain, the uncertainty reduction

Deleted: 1)

Deleted: 2)

Deleted: 3) improved

Deleted: the estimate of

shows no seasonal variability. The effect of decreasing the correlation length of the prior uncertainty, or of reducing the transport model errors compared to their present configuration (when conducting real-data inversion cases) can be larger than that of the extension of the measurement network in areas where the 23 stations observation network is the densest. We show that with a configuration of the ICOS atmospheric network containing 66 sites that can be expected on the long-term, the uncertainties in two-week mean NEE will be reduced by up to 50-80 % for countries like Finland, Germany, France and Spain, which could bring a significant improvement of (and at least a high complementarity to) our knowledge about NEE derived from biomass and soil carbon inventories at multi-annual scales.

Deleted: contrast

Deleted:

1 Introduction

Accurate information about the terrestrial biogenic CO_2 fluxes (hereafter Net Ecosystem Exchange - NEE) is needed at the regional scale to understand the drivers of the carbon cycle (Ciais et. al., 2014). Accounting for the natural fluxes in political agreements regarding the reduction of the CO_2 emissions requires their accurate quantification over administrative areas, and in particular over countries and smaller regional scales at which land management decisions can be implemented.

Deleted: .

Atmospheric inversions, which exploit atmospheric CO_2 mole fraction measurements to infer information about surface CO_2 fluxes (Enting, 2002) are expected to deliver robust and objective quantification of NEE at high temporal and spatial resolution over continuous areas and time periods. Global atmospheric inversions have been widely used to document natural carbon sources and sinks (Gurney et al., 2002, Rodenbeck et al., 2003). However, the spread of the results from the different global inversion studies and the diagnostics by some of these studies demonstrate that the uncertainty remain large at the one month and continental scale (Peylin et al., 2013). Such large uncertainties are mainly due to the lack of observations over the continents

Deleted:), although

Deleted: ,

Deleted: thus, likely

Deleted: (which is confirmed when it is diagnosed by the inversion studies),

85 or to the limited ability of global systems to account for dense observation networks in addition
86 to errors in large-scale atmospheric transport models. However, with an increasing number of
87 continuous atmospheric CO_2 observations, primarily in North America and Europe, and with the
88 development of regional inversion systems using high resolution mesoscale atmospheric
89 transport models and solving for NEE at typical resolutions of 10 to 50 km (Lauvaux et al., 2008,
90 2012, Schuh et al., 2010, Broquet et al., 2011, Meesters et al., 2012), there is an increasing
91 ability to constrain NEE at continental to regional scales.

92 This paper aims at studying the skill of a regional inversion system in Europe, which is equipped
93 with a relatively large number of ground-based atmospheric measurement stations, for estimating
94 NEE at the continental and country scales, down to 0.5° resolution (which is the resolution of the
95 transport model used in the inversion system). It also aims at assessing and comparing the
96 benefits from the measurement network extensions and from future improvement in the
97 inversion system. Such improvement can be anticipated either due to better atmospheric
98 transport models or to the use of better flux estimates as the prior information that gets updated
99 by the inversion based on the assimilation of atmospheric measurements.

100 Europe is a difficult application area for atmospheric inversion because of the very
101 heterogeneous distribution of vegetation types, land use, and agricultural and industrial activities
102 inside a relatively small domain, and, consequently, because of the need for solving for fluxes at
103 high resolution. Furthermore, its complex terrain also requires a high resolution of the
104 topography when modeling the atmospheric transport (Ahmadov et al., 2009). However, the
105 Integrated Carbon Observing System (ICOS) infrastructure is setting up a dense network of
106 standardized, long-term, continuous and high precision atmospheric and flux measurements in
107 Europe, with the aim of understanding the European carbon balance and monitoring the
108 effectiveness of Greenhouse Gas (GHG) mitigation activities (http://www.icos-
109 infrastructure.eu/). The atmospheric network is expected to increase from an initial configuration

of around 23 stations where actual measurements have been conducted during the past five years (even though all these sites will not necessarily be included in the official ICOS network in the coming years) up to around 60 stations in the near future (see ICOS Stakeholder handbook 2013 at https://icos-atc.lsce.ipsl.fr/?q=doc_public). In this context, the developers of the ICOS atmospheric network have encouraged network assessment studies such as the one conducted in this paper.

Several inversion studies have focused on the estimate of European NEE based on measurements from the CarboEurope-IP atmospheric stations, most of which are planning to join the ICOS atmospheric network (Peters et al., 2010, Broquet et al., 2011). Broquet et al. (2013) have demonstrated, based on comparisons with independent flux tower measurements, that there is a high confidence in the Bayesian estimate of the European NEE and of its uncertainty at the 1-month and continental scale based on their variational system which uses the CHIMERE mesoscale transport model run at 0.5° resolution. The distributions of the misfits between 1 month and continental scale averages of the flux measurements and of the NEE estimates sampled at the flux measurement locations were shown to be unbiased and consistent with the estimate of the uncertainties from the inversion system. This gives confidence in the inversion configuration of Broquet et al. (2011, 2013) for the estimation of the performance of the ICOS network. In particular, it gives confidence in their assumptions that the distribution of the uncertainties are unbiased and Gaussian, and that the impact of the uncertainties in the CO_2 modeling domain boundary conditions at the edges of Europe, and in the CO_2 fossil fuel emissions is weak (when assimilating measurements from the type of sites that form the ICOS network).

Here, we apply the system of Broquet et al. (2011, 2013) to assess the potential of the near term and realistic future configurations of the ICOS continuous measurements of CO_2 dry air mole fraction to improve NEE estimates at the mesoscale across Europe. This assessment is based on a

Deleted: (most existing today, hereafter ICOS23

Deleted: actual

Deleted: to

Deleted: Indeed, the

Deleted: revealed

Deleted: this system, described in

Deleted:), and in the underlying

Deleted: (e.g. on

Deleted: unbiased and Gaussian

Deleted: , or regarding the weak

Deleted: or

Deleted:) for

Deleted: estimation

Deleted: the performance of

Deleted: .

Deleted: Therefore, here

Deleted: of

153 quantitative evaluation of the uncertainties in the inverted fluxes (also called posterior
154 uncertainties) which are compared to the uncertainties in the prior information on NEE used by
155 the inversion system.

156 The Bayesian statistical framework chosen here provides estimates of the posterior uncertainties
157 as a function of the prior uncertainties, of the atmospheric transport and of the combination of
158 statistical errors which are not controlled by the update of the prior NEE by the inversion (like
159 the measurement errors and the atmospheric transport errors). Even though the prior uncertainty
160 can potentially depend on the value of the prior NEE, the actual values of the prior NEE or of the
161 measurement data to be assimilated are not formally involved in the estimation of the posterior
162 uncertainty due to the linearity of the atmospheric transport of CO_2. Therefore, the posterior
163 uncertainty can be derived for hypothetical observation networks or for hypothetical
164 uncertainties in the prior information or from the atmospheric transport model (i.e., for
165 hypothetical improvements in the prior information or in the atmospheric transport model) using
166 an Observing System Simulation Experiment (OSSE) framework, in which the results do not
167 depend on a simulated truth. Due to the dimension of the problem, uncertainties are not derived
168 analytically in this study and we use a Monte Carlo ensemble approach.

169 Using synthetic data in an OSSE framework has been a common way to assess the utility of new
170 GHG observing systems for the monitoring of the GHG sources and sinks at large scales based
171 on global inversion systems with coarse resolution transport models (e.g., Rayner et al., 1996,
172 Houweling et al., 2004, Chevallier et al., 2007, Kadygrov et al., 2009, Hungershoefer et al.,
173 2010). This approach now plays a critical role in the recent emergence of regional inversion
174 systems supporting strategies for the deployment of regional observation networks and assessing
175 the potential of regional inversion for assessing the GHG fluxes at a relatively high resolution
176 (Tolk et al., 2011, Ziehn et al., 2014). Such a use of OSSEs today is not specific to the GHG
177 inversion community. OSSEs are increasingly used by the air quality community (e.g., Edwards

et al., 2009, Timmermans et al. 2009a, b, 2015, Claeyman et al., 2011) and they are still extensively used by the meteorological community (e.g., Masutani et al., 2010, Riishøjgaard et al., 2012, Errico et al., 2013, see also https://www.gmes-atmosphere.eu/events/osse_workshop/).

In these areas, twin experiments are often used to derive a single realization of the uncertainties (Masutani et al., 2010) while our Monte Carlo approach explores the uncertainty space much more extensively. Further, in common (linear) CO_2 atmospheric inversions, since the results are independent of the synthetic "true" data used for the OSSE, any simulation can be used to build this truth, while, when using fraternal twin experiments with nonlinear models in other application fields of data assimilation, it is critical to ensure that the truth is realistic enough (Halliwell et al., 2014). The reliability of the OSSEs in CO_2 atmospheric inversion critically depends on the realism of their input error statistics since their configuration in the inversion system is perfectly consistent with the sampling of synthetic errors that are used in these experiments. In this study, our confidence in the realism of the statistical modeling approach and of the input error statistics, and thus in the inversion set-up, is based on the statistical modeling studies of Chevallier et al. (2012) and Broquet et al. (2013) that were themselves based on real data.

The manuscript first documents the potential for constraining NEE, through the use of a state-of-the-art, i.e., which solves the NEE at high spatial and temporal resolution, and which has been submitted to a high level of evaluation, variational atmospheric inversion system, and of the ICOS23 network containing existing sites and other stations that could be installed on tall towers over Europe in the coming years. We also consider two longer-term ICOS configurations with 50 stations (hereafter ICOS50) and 66 stations (hereafter ICOS66). For the time domain, we consider results for NEE aggregated at the two-week scale, for two different periods of the year (in July and in December). Shorter aggregation scales, like a day, result in a significant dependency of NEE to specific synoptic events. Longer time scales require computing resources

Deleted: Riishojgaard

Deleted: fields

Deleted: Still, the

Deleted: (

Deleted: .

Deleted:)

Deleted:), respectively.

Deleted: the

Deleted: imply

212 that are beyond the scope of this study with this high-resolution inversion system. We pay
213 special attention to the analysis of the results at different spatial scales, from the native transport
214 model grid scale of about 50x50 km^2 up to the national scale that is the most relevant for
215 supporting environmental policy, and the full European domain considered in this study (which
216 extends to western Russia and Turkey). We also present the sensitivity of our results to
217 parameters characterizing the future developments of the mesoscale inversion systems: the
218 reduction of the transport model errors or of the prior flux errors.

219 The paper is organized as follows. Section 2 describes the mesoscale inversion experimental
220 framework focusing on the Monte Carlo estimate of uncertainties. Section 3 analyses the scores
221 of posterior uncertainties and the uncertainty reduction compared to the prior uncertainties in
222 order to assess the potential of the near term framework and the one of future improvements of
223 the network or of the inversion set-up. The last section synthesizes the results and discusses
224 them.

225

226 **2 Materials and Methods**

227 **2.1 The configurations of the ICOS atmospheric observation network**

228 We consider three successive phases of deployment of the ICOS atmospheric network. The
229 initial state ICOS23 configuration includes 23 sites among which there are eight tall towers. This
230 minimum network configuration is based on existing stations, most of them being operational in
231 the CarboEurope-IP FP6 project. The ICOS network is expected to further expand during the
232 next 5 years according to the country declarations at the ICOS Interim Stakeholder Council and
233 to the ICOS European Research Infrastructure Consortium 5 year financial plan. Using possible
234 locations for the future stations, including sites that have already been discussed with the ICOS
235 consortium during the ICOS preparatory phase FP7 project (European Union's Seventh Research

Deleted: (

Deleted:).

Framework Programme, grant agreement No. 211574), we derived two plausible ICOS configurations: ICOS50 with 50 sites including 24 tall towers and ICOS66 with 66 sites including 33 tall towers.

The locations and details on the sites of the three configurations are summarized in Table A1 and in Fig. 1. Here, the existing and future ICOS CO_2 observations are assumed to comply with the World Meteorological Organization (WMO) accuracy targets of 0.1 parts per million (ppm) measurement precision (WMO, 1981, Francey, 1998) so that the measurement error is negligible in comparison to the other type of errors that have to be accounted for in the inversion framework such as the model transport and representation errors (see their typical estimate in Sect. 2.2.2).

2.2 Mesoscale inversion system

2.2.1 Method

The estimate of uncertainties related to the different ICOS networks is based on an ensemble of inversions with the variational inversion system of Broquet et al. (2011), assimilating synthetic hourly averages of the atmospheric CO_2 data from these networks (during the afternoon or during nighttime only, depending on the type of sites that are considered, see Sect. 2.2.2.). A regional atmospheric transport model (see its description below) is used to estimate the relationship between the CO_2 fluxes and the CO_2 mixing ratios. The inversion system solves for 6-hour mean NEE on each grid point of the 0.5º by 0.5º resolution grid used for the transport modeling. It also solves for 6-hour mean ocean fluxes at 0.5° spatial resolution in order to account for errors from air-sea fluxes when mapping fluxes into hourly mean mixing ratios. However, analyzing the uncertainty reduction for ocean fluxes is out of the scope of this paper.

Deleted: over restricted time windows everyday

Peylin et al. (2011) indicate that uncertainties in anthropogenic fluxes yield errors when simulating CO_2 mixing ratios at ICOS stations that are smaller than atmospheric model errors. Furthermore, the relative uncertainty in anthropogenic emissions is smaller than that in NEE, while on short timescales, the anthropogenic signal is generally smaller than the signature of the NEE at sites that are not very close (typically at less than 40km) to strong anthropogenic sources such as cities (see the analysis for the Trainou ICOS station near Orléans, in France by Bréon et al. 2015). Relying on such indications, we assume that the errors due to uncertainties in anthropogenic emissions are negligible compared to errors from NEE and atmospheric model errors. This is a reasonable assumption as long as most ICOS stations are relatively far from large urban areas, which should be the case since the ICOS atmospheric station specification document (https://icos-atc.lsce.ipsl.fr/?q=doc_public) recommends that the measurements sites are located at more than 40km from the strong anthropogenic sources (such as the cities). Zhang et al. (2015) yield conclusions from their transport experiments at 1° resolution which contradict this assumption and this clearly raises an open debate. However, the evaluation of the inversion configuration from Broquet et al. (2013) supports our use of this assumption for our study.

In order to simulate the full amount of CO_2 in the atmosphere, the inversion uses a fixed estimate of the fossil fuel emissions (see below) without attempting to correct it nor account for uncertainties in these fluxes. The inversion also uses a fixed estimate of the CO_2 boundary conditions at the lateral and top boundaries of the regional modeling domain without attempting to correct it nor account for uncertainties in these conditions. This follows the protocol from Broquet et al. (2011) which assumed that the error from the boundary conditions for the European domain is mainly a bias and which corrects for such a bias in a preliminary step that is independent to the subsequent application of the inversion. Such an assumption is supported by the evaluation of the inversion configuration by Broquet et al. (2013). The relatively weak impact of uncertainties in the boundary conditions in Europe (while studies in other regions such as that of Gockede et al. (2010) indicate a high influence of such uncertainties) can be explained

Deleted: fair

Deleted: Therefore, in

Deleted: at correcting

Deleted: at accounting

Deleted: at correcting

Deleted: or at accounting

Deleted: Again such

by the fact that the spatial scale of the incoming CO_2 patterns at the ICOS sites from remote sources and sinks outside the European domain boundaries is relatively large due to atmospheric diffusion (especially under west wind conditions, when the air comes from the Atlantic ocean) compared to the typical distances between the ICOS sites. In principle, the inversion mainly exploits the smaller scale signal of the gradients between the sites to constrain the NEE, and it is thus weakly influenced by the large scale signature of the uncertainty in the boundary conditions. In this section we only summarize the main elements of the inversion system, starting with the theoretical framework, while the detailed description can be found in Broquet et al. (2011).

We define the control vector $\boldsymbol{x}$ of the atmospheric inversion as the 6-hour and 0.5°x0.5° mean NEE and ocean fluxes. The atmospheric inversion seeks the mean $\boldsymbol{x}_a$ and covariance matrix $\mathbf{A}$ of the normal distribution $N(\boldsymbol{x}_a, \mathbf{A})$ of the knowledge on $\boldsymbol{x}$ based on (i) the atmospheric transport model, (ii) the prior knowledge $\boldsymbol{x}_b$ of $\boldsymbol{x}$, (iii) the hourly mean atmospheric measurements $\boldsymbol{y}$, (iv and v) the covariances $\mathbf{B}$ and $\mathbf{R}$ of the distributions of the prior uncertainty and of the observation error assuming that these uncertainties are normal and unbiased (i.e., equal to $N(0, \mathbf{B})$ and $N(0, \mathbf{R})$ respectively), and (vi) a Bayesian relationship between these distributions. The observation error is the combination of all sources of misfit between the atmospheric transport model and the concentration measurements other than the prior uncertainty, in particular the measurement errors, the model transport, aggregation and representation errors, and the errors from the model inputs that are not controlled by the inversion.

With this theoretical framework, $\boldsymbol{x}_a$ is the minimum of the quadratic cost function $J(\boldsymbol{x})$ (Rodgers, 2000):

$$J(\boldsymbol{x}) = \frac{1}{2}(\boldsymbol{x} - \boldsymbol{x}_b)^T \mathbf{B}^{-1}(\boldsymbol{x} - \boldsymbol{x}_b) + \frac{1}{2}(H(\boldsymbol{x}) - \mathbf{y})^T \mathbf{R}^{-1}(H(\boldsymbol{x}) - \boldsymbol{y}) \qquad (1)$$

where ^{T} denotes the transpose, and where H is the affine observation operator which maps the 6-hour (00:00-06:00, 06:00-12:00, 12:00-18:00 and 18:00-24:00; UTC time is used hereafter) and

Deleted: the

0.5° × 0.5° mean NEE and ocean CO_2 fluxes $\boldsymbol{x}$ to the observational space based on the linear CO_2 atmospheric transport model with fixed open boundary conditions, and with fixed estimates of the anthropogenic fluxes and natural fluxes at resolutions higher than 6-hour and 0.5°; *H:* $\boldsymbol{x}$ -> $H(\boldsymbol{x})$ can be rewritten H: $\boldsymbol{x} \rightarrow \mathbf{H}\boldsymbol{x} + \boldsymbol{y}_{fixed}$ where $\boldsymbol{y}_{fixed}$ is the signature, through atmospheric transport, of the fluxes (in particular the anthropogenic emissions) and boundary conditions not controlled by the inversion. **H** is the combination of two linear operators: the first operator distributing 6-hour mean natural fluxes at the 1-hour resolution, and the second operator simulating the atmospheric transport from the 1-hour resolution fluxes at 0.5° resolution.

The inversion system derives an estimate of $\boldsymbol{x}_a$ by performing an iterative minimization of $J(\boldsymbol{x})$ with the M1QN3 algorithm of Gilbert and Lemaréchal (1989). The gradient of J is derived using the adjoint operator of **H** thanks to the availability of the adjoint version of the CHIMERE code. The covariance of the posterior uncertainty in inverted NEE **A**, of main interest for this study, is given by the formula:

$$\mathbf{A} = (\mathbf{B}^{-1} + \mathbf{H}^{\mathbf{T}}\mathbf{R}^{-1}\mathbf{H})^{-1} \quad (2)$$

This equation demonstrates the point raised in the introduction for justifying the OSSE framework, that **A** does not depend on the observations or on the prior flux values themselves but only on their error covariance matrices, on the observation network density and station location, and on the atmospheric transport operator. This allows assessing the performance of any observation system, whether existing or not. Of note is also that this calculation does not depend on $\mathbf{y}_{fixed}$, i.e., on the boundary conditions or on the anthropogenic fluxes in the domain so that such components can be ignored for the estimate of **A**.

In this framework, a common performance indicator is the theoretical uncertainty reduction for specific budgets of the NEE estimates (averages over specified periods of time and over specified spatial domains), defined by:

Deleted: stations

$$\gamma = 1 - \frac{\sigma_a}{\sigma_b} \qquad (3)$$

where σ_a and σ_b are the standard deviations of the posterior and prior uncertainties in the corresponding integrals in time and space (over the given periods of time and spatial domains) of the 6-hour and 0.5° resolution NEE field. If the observations perfectly constrain the inversion of a given budget of NEE, then γ = 1. If the observations do not bring any information to reduce the error from the prior, $\gamma = 0$. By definition, γ is a quantity relative to the uncertainty in the prior fluxes, which depends on the type of prior information on NEE that is expected to be used (estimates from a biosphere model in our case, see below Sect. 2.2.2). Of note is that the scores of uncertainty and of uncertainty reduction given in this study refer to the standard deviation of the uncertainty in a specific budget of NEE, and that, hereafter, the term "standard deviation" is generally omitted.

Due to the size of the observation and control vectors in this study, we could not afford the analytical computation of Eq. (2) based on the full computation of the **H** matrix using a very large number of CHIMERE simulations; Hungershoefer et al. (2010). Instead we use the Monte Carlo approach of Chevallier et al. (2007) to compute **A**. In this approach, an ensemble of posterior fluxes $\boldsymbol{x}_{ai}$ is derived from an ensemble of inversions using the synthetic prior flux $\boldsymbol{x}_{bi}$ and data $\boldsymbol{y}_i$ whose random errors ($\boldsymbol{x}_{bi}$-$\boldsymbol{x}_{true}$ for $\boldsymbol{x}_{bi}$ and $\boldsymbol{y}_i$-$\mathbf{H}\boldsymbol{x}_{true}$ for $\boldsymbol{y}_i$) with respect to a known truth ($\boldsymbol{x}_{true}$, whose value does not influence the results analyzed here, and which is thus ignored hereafter) sample the distributions $N(0, \mathbf{B})$ and $N(0, \mathbf{R})$. **A** is obtained as the statistics of the posterior errors $\boldsymbol{x}_{ai}$-$\boldsymbol{x}_{true}$. The practical size of the ensemble is described below and its determination follows the discussion by Broquet et al. (2011). The convergence of the estimate of the inverted NEE for each inversion and the convergence of the statistics of the ensemble are necessary to ensure that the **A** matrix computed with this method corresponds to the actual covariance of the posterior uncertainty given by Eq. (2). These convergences cannot be perfect with a limited number of iterations for the minimization algorithm and a limited number of

Deleted: On
Deleted: opposite, if it does
Deleted: (
Deleted: ,
Deleted: respectively)

inversion experiments in the Monte Carlo ensemble imposed by computational limitations. Therefore the estimate of **A** can depend on parameters other than **H**, **B** and **R** in practice, i.e., the number of iterations and of inversion experiments. However, it has been checked (see below Sect. 2.2.2) that the convergence is sufficient so that this dependence should not be significant for the quantities of interest.

Deleted: numbers

2.2.2 Practical set-up

Atmospheric transport model

In this study, the operator **H** is based on the CHIMERE mesoscale atmospheric transport model (Schmidt et al., 2001) forced with European Centre for Medium-Range Weather Forecasts (ECMWF) winds. We use a configuration with a 0.5ºx0.5º horizontal grid and with 25 σ-coordinate vertical levels starting from the surface and with a ceiling at ~500 hPa (such a ceiling being usual for regional transport modeling when focusing on mole fractions close to the ground, e.g. Marécal et al. 2015). The spatial extent of the corresponding domain is described below. CHIMERE is an off-line transport model. Hourly mass-fluxes are provided by the analyses of the ECMWF. The relatively high vertical and horizontal resolutions of CHIMERE allow a good vertical discretization of the Planetary Boundary Layer (PBL; the first 14 levels are below 1500 meters) along with a good representation of the orography and dynamics to match high frequency observations better than with a global configuration whose typical horizontal resolution is ~3° (Peylin et al. 2013).

Deleted: European Centre for Medium-Range Weather Forecasts (ECMWF).

Spatial and temporal domains

In this study, we use the European domain shown in Fig. 1a which covers most of the European Union and some of Eastern Europe, with a land surface area of 6.8×10^6 km^2. Its southwest corner

is at 35ºN and 15ºW, and its northeast corner is at 70ºN and 35ºE. Two temporal windows are considered, from June 30, 2007 to July 20, 2007 and from 2 to 22 of December 2007 (of almost three weeks each). The choice of these periods of three weeks is a tradeoff between widening the scope of the study and computational burden. The Monte Carlo-based flux uncertainty reduction calculations require large computing resources, while we test three different network configurations for two different months, and for different setups of the error covariance matrices. Three week experiments allow retrieving information about uncertainties at the two-week scale without being biased by edge effects, i.e., they allow accounting for the impact of uncertainties from the days before the 14 targeted days and for the impact of the assimilation of measurements during the days after these 14 targeted days. The advection of CO_2 throughout Europe can last more than three days, but atmospheric diffusion ensures that the signature at ICOS sites of the NEE during a 6-hour window is generally negligible after three days of transport (not shown). Thus, the windows 3-17 July and 5-19 December were chosen for analysis respectively. We consider the results for July and December to be representative for the summer and winter seasons (using the name of the seasons for the Northern Hemisphere hereafter), allowing an analysis of seasonal variations of the flux uncertainty reduction. Choosing year 2007 for the period of the inversion only impacts the meteorological conditions (i.e., the impact on the prior uncertainty whose local standard deviations are scaled using data from this specific year, as detailed below in this section, is negligible) and thus the atmospheric transport conditions in the OSSEs. We assume that these conditions are not impacted by a strong inter-annual anomaly in 2007 so that they can be expected to be representative of average conditions for summer and winter. Hereafter, the mention of the year 2007 is thus often ignored and we assume that we retrieve typical estimates for July and December.

Deleted: those

Deleted: Indeed, the

Deleted: the

Deleted: ,

Deleted: in the structure

Flux error covariance matrix

The set-up of the error covariance matrix **B** follows the methodology of Chevallier et al. (2007). It is chosen to represent the typical uncertainty in estimates from the biosphere models (for NEE) and from climatologies (for ocean fluxes) used by traditional atmospheric inversion systems. The statistics have been derived for estimates from the Organising Carbon and Hydrology In Dynamic Ecosystems (ORCHIDEE) vegetation model (Krinner et al., 2005) and the ocean climatology from Takahashi et al. (2009). The uncertainties in NEE are assumed to be autocorrelated in space and in time and are modeled using isotropic and exponentially decreasing functions with correlation lengths that do not depend on the time or location. A Kronecker product of the matrices of temporal and spatial correlations ensures the combination of these two types of correlations. The e-folding spatial and temporal correlation lengths are set according to the estimation of Chevallier et al. (2012) based on comparison of the NEE derived by the ORCHIDEE model and eddy-covariance flux tower data, for our specific prior flux spatial and temporal resolution, i.e., to 30 days in time and 250 km in space over land. NEE uncertainties for different 6-hour windows of the day are not correlated, i.e., the temporal correlations only apply to a given 6-hour window of consecutive days. The standard deviations of the prior uncertainties in **B** are set proportionally to the heterotrophic respiration fluxes from the ORCHIDEE model (it is approximately twice this respiration at the daily and 0.5° scale). We apply time-dependent scaling factors to these fluxes so that the NEE uncertainties have lower values during the night than during the day, and during winter than during summer, summing up to typical values for grid-scale and daily errors ~ 2.5 $gCm^{-2}day^{-1}$ in summer (maximum value 3.4 $gCm^{-2}day^{-1}$) and ~ 2 $gCm^{-2}day^{-1}$ in winter (maximum value 3.1 $gCm^{-2}day^{-1}$). Over the ocean, the prior uncertainty of air-sea fluxes has standard deviations at the 0.5° and 6-hour scale equal to 0.2 $gCm^{-2}day^{-1}$, an e-folding spatial correlation length of 500 km and temporal correlations similar to those for the prior uncertainties over land. Prior ocean and land flux uncertainties are not correlated.

Deleted: setup

Deleted: more specifically

Deleted: that

461 **Time selection of the data to be assimilated**

462 Broquet et al. (2011) analyzed the periods of time during which the CHIMERE European
463 configuration bears transport biases which are too high so that measurements from ground based
464 stations such as ICOS sites should not be assimilated to avoid projecting erroneously such biases
465 into the corrections to the fluxes. In agreement with common practice, they concluded that
466 observations at low altitude sites (approximately below 1000 meters above sea level (masl); see
467 Broquet et al. (2011) for the exact definition of the different types of sites used for the time
468 selection of the data and the configuration of the observation error) which include almost all of
469 the ICOS tall towers, should be assimilated during daytime (12:00-20:00) while the observations
470 at high altitude stations (approximately above 1000 masl) should be used during the night
471 (00:00-06:00) only. This generally yields larger uncertainty reduction during daytime than
472 during nighttime (Broquet et al. 2011). However, this does not raise a potential bias related to a
473 better constrain on daytime inverted NEE (when the ecosystems are generally a sink of CO_2)
474 than on nighttime inverted NEE (when the ecosystems are generally a source of CO_2) since
475 uncertainties in both nighttime and daytime prior NEE, transport and measurements are assumed
476 to be unbiased, as supported by the results from Broquet et al. (2013).

Deleted: only

477

478 **Observation error covariance matrix**

479 The observational error covariance matrix **R** accounts for various sources of error when
480 comparing the hourly data selected for assimilation and their simulation which are not controlled
481 by the inversion: measurement error, aggregation error, atmospheric model representativeness
482 and transport error (as explained previously, uncertainties in the anthropogenic emissions and in
483 the boundary conditions are assumed to be negligible). The first two terms are negligible
484 compared to the model representativeness and transport error due to the high measurement

standard and to solving for the fluxes at 6-hour and 0.5° resolution during the inversion, respectively.

Broquet et al. (2011) derived a quantitative estimation of the model error (depending on the station height) including transport and representativeness errors based on comparisons between simulations and measurements of CO_2 and ^{222}Rn during summer. Broquet et al. (2013) extended this analysis using 1-year long timeseries of simulated and measured CO_2 and ^{222}Rn, to provide season-dependent estimates which are used here. The model error is much higher during the winter than that during the summer. It is given for each site in Table A1 for the two months (July, December) considered in this study. We assume that the errors for two different sites are independent and that they do not bear temporal autocorrelations. Thus, the observation error covariance matrix **R** is set diagonal. There is no evidence that such autocorrelations could be significant in the analysis of Broquet et al. (2011). The resulting budget of observation errors at daily to monthly resolution seems reliable (Broquet et al. 2011, 2013). This may confirm that the temporal auto-correlations of the actual observation errors are negligible. If the auto-correlations of the actual observation errors were not negligible, this would mean that the errors for hourly data are overestimated. In both cases, the assumption that the temporal autocorrelations of the observation error are negligible does not seem to need to be balanced by an artificial increase of the estimate of the observation errors for hourly averages from Broquet et al. (2013).

Deleted: .

Deleted: resumed it

Deleted: Indeed, there

Deleted: It could be due either to a compensation of ignoring the temporal autocorrelations by an overestimate of errors for hourly data, or to the fact

Deleted: (Broquet et al. 2013). However, in

Deleted: .

Minimization and number of members in the Monte Carlo ensembles

We use 12 iterations of minimization for each variational inversion of the Monte Carlo ensemble experiments. This number is similar to that from Broquet et al. (2011) where they considered a longer time period for the inversions but far smaller observation networks and a smaller inversion domain, which reduces the dimensions of the minimization problem. However, here, 12 iterations were still found to be sufficient for converging toward the theoretical minimum of

521 the cost function, i.e., the number of assimilated data divided by two (Weaver et al., 2003), with
522 less than 10% relative difference to this theoretical minimum except for a few cases (for these
523 cases, 18 iterations were used to reach a relative difference to the theoretical minimum that is
524 smaller than 10%).

525 Similarly to Broquet et al. (2011), 60 members are used in each Monte Carlo ensemble
526 experiment. This is also the typical number of members that Bousserez et al. (2015) use for their
527 Monte Carlo simulations. Broquet et al. (2011) found a satisfactory convergence of the estimate
528 of the uncertainties in Europe and 1-month average NEE with an ensemble size of 60, which is
529 confirmed here (the estimates using 50 and more members are within 6% of the results with 60
530 members).

Deleted: (this

Deleted:)." ¶
. They

Deleted: ,

Deleted: such a

Deleted: the ensemble

531

532 **2.2.3 Sensitivity tests**

533 Three and five Monte Carlo ensembles of inversions are conducted for December and July
534 respectively. For each season, 3 ensembles using the default set-up of **B** and **R** described above
535 are conducted in order to give results for the 3 different ICOS network configurations and
536 consequently the sensitivity to the network configuration. In July, two ensembles are also
537 conducted with a change in **R** in one case and in **B** in the other case in order to test the sensitivity
538 to these inversion parameters. Such sensitivity tests have been conducted in July only and using
539 one configuration of the ICOS network only (ICOS50 and ICOS66 for the test of sensitivity to **R**
540 and **B** respectively) since a more exhaustive set of tests of sensitivity for the two seasons and for
541 each ICOS network configuration was not expected to bring new insights while raising
542 significant additional computation costs. The set-up of the inversion for these two sensitivity
543 tests is now described.

544

551 **Test of the sensitivity to the observation error**

552 There is a steady increase in the resolution of the atmospheric transport models used for
553 atmospheric inversions, with corresponding improvements of the simulation precision (e.g., Law
554 et al. 2008). In this test we simulate the effect of potential future transport model improvement
555 on the posterior flux uncertainties by reducing the default observation error standard deviations
556 in **R** by a factor of two. This factor roughly corresponds to the improvement of the misfits
557 between the model and actual measurement at the site TRN (see Fig. 1 for its location), that was
558 observed when bringing CHIMERE from the current 0.5° resolution down to a 2 km resolution
559 using the configuration presented in Bréon et al. (2014). The underlying assumption would be
560 that ~1km horizontal resolution atmospheric transport models could be used for inversions at the
561 European scale in the near future. Hereafter, we denote by $\mathbf{R}_{ref}$ the reference configuration of **R**
562 and by $\mathbf{R}_{red}$ the one corresponding to reduced standard deviations.

563

564 **Test of the sensitivity to the prior uncertainty**

565 The test of the sensitivity of the inversion system to the prior uncertainty is focused on that of the
566 sensitivity to the spatial correlation length in **B** (Gerbig et. al. 2006) (which impacts the budget
567 of uncertainty over large regions). The possible use of better prior flux fields based on the
568 merging of both estimates from vegetation models and from large scale inventories (such as
569 forest and agricultural inventories) can be expected to generate smaller-scale uncertainties than
570 when using vegetation models while it is not obvious that local uncertainties would be decreased
571 when adding information from inventories (since inventories only measure long term integrated
572 NEE). Therefore, we tested the impact of reducing the spatial correlation length for the prior
573 uncertainty in NEE from 250 km to 150 km, denoting hereafter the corresponding configurations
574 for the **B** matrix: $\mathbf{B}_{250}$ and $\mathbf{B}_{150}$ respectively.

3. Results and discussion

3.1 Assessment of the performance of the actual network and system

In this section, the performance of the inversion relying on the default configuration and on the ICOS23 initial state network (i.e., the reference inversion) is analyzed as a function of the spatial scale, highlighting the main patterns of the uncertainty reduction obtained from the pixel scale to the regional (national, European) scales.

Deleted: at

Deleted: scale

3.1.1 Analysis at the model grid scale

Figures 2a and 2b show the uncertainty reduction for estimates of two-week average NEE at 0.5º resolution in July and December, respectively. This grid-scale uncertainty reduction reaches 65% for areas in the vicinity of the ICOS sites and decreases smoothly with distance away from measurement sites. For most of the area around eastern France – western Germany, this grid – scale uncertainty reduction ranges from 35 to 50% for July and from 20 to 40% for December. This stems from the combination of the dense observation network over that region, and from the 250 km correlation scale for the prior uncertainties, which spreads the error reduction beyond the immediate vicinity of each station where near field fluxes have a large influence on the mixing ratio at this station (Bocquet, 2005). For other parts of Europe that are not well sampled by ICOS, significant uncertainty reductions are generally seen around each site but there are large areas where the inversion has no impact at the grid scale: Scandinavian countries, the eastern part of Germany, Poland, the south of the Iberian Peninsula and almost all of Eastern Europe.

The spatial structure of the uncertainty reduction and the underlying spatial extrapolation from a site is a complex combination of transport influence and of the structure of the prior uncertainty. Due to varying transport conditions, standard deviation of the prior uncertainty at the grid scale

601 (which is larger in summer, see below the comments on Fig. 3), and observation error (which is
602 larger in winter), the spatial distribution of uncertainty reduction is found to vary from summer
603 to winter. Because the prior uncertainties are larger and the observation errors are smaller in July
604 than in December, there is generally a larger uncertainty reduction in July (especially in Western
605 Europe). But variations in meteorology alter (limiting or enhancing) this general behavior. The
606 lower vertical mixing (which strengthens the sensitivity of the near ground measurements to the
607 local fluxes) partly balances the higher observation error in December and the range of local
608 uncertainty reductions overlaps between July and December. The observations from the Angus
609 tall tower (**tta** site, Table A1) in Scotland or from Pallas (**pal** site, Table A1) in Finland
610 contribute differently to the uncertainty reduction during July and December (using
611 meteorological conditions from 2007), showing better performance at the grid scale during
612 summer. This also comes from the different weather regimes, with different dominant wind
613 directions, different average wind speed and different vertical mixing in summer and winter.
614 Regions lacking stations in ICOS23 have an uncertainty reduction which is more sensitive to the
615 atmospheric transport than regions with a dense network. The uncertainty reduction in December
616 is significantly larger in the east and in the southeast part of domain compared to July, due to
617 more occurrences of winds from the east during December than during July.

618 Complementing the uncertainty reduction, Fig. 3 shows prior and posterior uncertainty standard
619 deviations at the grid scale in order to illustrate the precision of the estimates of NEE that should
620 be achievable with the reference inversion using the ICOS23 network. As already stated, prior
621 uncertainties are up to ~3 $gCm^{-2}day^{-1}$ (Fig. 3a) but the winter values are smaller than the summer
622 ones (due to a weaker activity of the ecosystems; Fig. 3b). During both July and December, the
623 uncertainties in two-week mean NEE in the regions that are best covered by observations (most
624 of Western Europe) at 0.5° resolution are reduced by the inversion down to typical values of ~
625 1.5 gCm^2day (Fig. 3c,d).

626

627 **3.1.2 Analysis at national scale**

628 Figures 4a and 4b show the uncertainty reduction for two-week-and country-mean NEE in July
629 and December respectively. The countries and corresponding estimates of prior and posterior
630 uncertainties are listed in Table A2. The results suggest the ability of the mesoscale inversion
631 framework to derive estimates of the NEE at the national scales with relatively low uncertainties.
632 The uncertainty reduction is particularly large for countries such as Germany, France and the UK
633 e.g., more than 80% for France during July. It is larger than 50% for a large majority of the
634 countries in Western Europe and Scandinavia both in July and December.

635 The smallest uncertainty reduction applies to southeastern European countries where it can be
636 smaller than 10 % (e.g., for Greece in July) indicating that the presence of stations very close to
637 or within a given country is a requisite for bringing significant improvement to the estimates of
638 NEE in this country. In general, the differences of the inversion skill between July and December
639 look consistent with what has been analyzed at the pixel scale. In particular the uncertainty
640 reduction is higher in July for western countries but higher in December for eastern countries for
641 the same reasons as that given when analyzing the same behavior at the pixel scale (see Sect.
642 3.1.1).

Deleted: .

643

644 **3.1.3 Analysis at the European scale**

645 Table 1 shows that the uncertainty in two-week-mean NEE in July averaged over the full
646 European domain (6.8×10^6 km^2 of land surface) is reduced by the inversion by 50% down to a
647 value of ~ 43 TgCmonth^{-1} (see Table 1 for details) using the default configuration. The
648 uncertainty reduction for December is 66%, resulting in a posterior uncertainty of ~26
649 TgCmonth^{-1}. The uncertainty reduction for the whole European domain is thus higher in

December than in July. More precisely, while easterly winds in December strongly favor this period in terms of uncertainty reduction in Eastern Europe, the uncertainty reduction for NEE averaged over the reduced western European domain defined in Fig. 1c does not vary significantly with the season (66% and 64% for July and December respectively). This lack of seasonal variation of the uncertainty reduction at the scale of the western European domain (where most of the ICOS23 stations are located) seems to contrast with the grid-scale and national scales estimations in this domain which indicates that the uncertainty reduction is generally significantly higher during summer than during winter. This contrast will be analyzed and interpreted in the Sect. 3.1.4.

Deleted: indicated

Deleted: following

3.1.4 Analysis of the variations of the uncertainty as a function of the spatial aggregation of the NEE: interpretation of the results obtained at the national and European scales

In order to examine here the dependency of the NEE uncertainty reduction to increasing spatial scales of aggregation for the analyses in July and December, we chose five locations at which we define centered areas with increasing size for which uncertainties in the average NEE are derived. These stations are located using the green circles in Fig. 1c. The five locations correspond to three observing sites of ICOS23: Trainou (TRN), Ochsenkopf (OXK), Plateau Rosa (PRS); one site of ICOS50: SMEAR II-ICOS Hyytiälä (HYY); and one point in Sweden which does not correspond to any site of the ICOS networks tested here, called SW1 hereafter (Fig. 1c). We compute the uncertainty reductions of the two-week mean NEE for July and December over five squares centered around each site and of increasing size (in square degrees): 1.5ºx1.5º, 2.5ºx2.5º, 3.5ºx3.5º, 4.5ºx4.5º and 10.5ºx10.5º respectively (which corresponds to surfaces of different size in terms of km^2). Depending on their location and on their size, the corresponding domains expand over areas of Europe that are more or less constrained by the inversion at the pixel scale. But the variations of the uncertainty reduction when increasing the

Deleted: 5 square (in degrees) domains

Deleted: of

Deleted: size

size of these domains are also strongly driven by the spatial correlations in the prior and posterior uncertainty. The results are displayed in Fig. 5.

The five locations used for this analysis are representative of the diversity of the situation regarding the differences between grid scale uncertainty reduction in July and in December. While the uncertainty reduction is slightly larger in July than in December for TRN, much larger in July for PRS and HYY, it is slightly larger in December at OXK and much larger in December at SW1. Furthermore, the values for these grid scale uncertainty reductions range from 15% to 50% in July and from 7% to 47% in December at these locations (Fig. 5).

The maximum scores of uncertainty reduction occur for spatial scales of aggregation ranging from 10^5 km^2 to 10^6 km^2 when considering the sites located in Western Europe. These scales approximately correspond to the range of the sizes of the European countries and it is larger than the typical area of correlation of the prior uncertainty (as defined by prior correlation lengths of 250 km). Increasing the spatial resolution generally increases the uncertainty reduction since posterior uncertainties have generally smaller correlation lengths than prior uncertainties, due to the spatial attribution error when trying to link the measurement information to local fluxes despite the atmospheric mixing. This explains the increase of uncertainty reduction from the grid scale to the "national scales". This also explains why, for a given regional density of the measurement network, larger countries bear larger uncertainty reductions (Fig. 4). However, above such national scales, the corresponding domains include parts of Eastern Europe being poorly sampled by the ICOS23 network which explains the decrease in uncertainty reduction.

The convergence between the results around TRN, PRS and OXK in December and July (which tend to nearly 65% uncertainty reduction when the averaging area reaches the western European domain), between the results around all sites in December (which tend to 66% uncertainty reduction when the averaging area reaches the whole Europe), or between the results around all sites in July (which tend to nearly 53% uncertainty reduction when the averaging area reaches

Deleted: of

Deleted: in both December and July for

Deleted: , and of

Deleted: at

Deleted: to 53% in July and 66%

Deleted: for

Deleted: , when increasing the spatial averaging area,

the whole Europe), starts between the 10^5km^2 and 10^6km^2 (national scale) averaging areas. For smaller areas, the differences between results in July and December or between results for different spatial locations stay similar to what is seen at the 0.5°x0.5° scale.

Deleted: same

The similarity of the results for the western European domain despite differences at the grid scale in July and December can be explained by differences of correlations between areas at scales similar or larger than the national scale in the posterior uncertainties (since the correlations of the prior uncertainties aggregated at the national scale or at larger scales are very close for July and December). Figure 6 illustrates the variations of such correlations of the posterior uncertainty at the national scale between July and December using the example of correlations between Germany and other countries. These correlations are usually more negative in December, which indicates a larger difficulty in December than in July to distinguish in the information from the measurement network the separate contributions of the different neighboring countries (or of different areas of larger size). This can be attributed to the stronger winds in December which increase the extent of the flux footprints of the concentration measurements. Such an increase of the footprints in December limit the ability to solve for the fluxes in the vicinity of the measurement sites but increase the ability to solve for the fluxes at large scales.

3.2 Impact of the extension of the ICOS network

The effect on local (grid scale) uncertainty reduction of assimilating data from new sites in the ICOS network depends on the coverage of the area by the initial ICOS23 network, as illustrated by the comparison of the results using ICOS23, ICOS50 and ICOS66 and the reference configuration of the inversion (see Figs. 2 and 7). For example, adding one new site in Sweden or Finland yields a stronger increase of the uncertainty reduction than adding one site in the central part of Western Europe, where the network is already rather dense. Since most of the new sites from ICOS23 to ICOS50 and then ICOS66 are located in Western Europe, the

Deleted: Fig

741 improvements due to adding 27 or 43 sites to ICOS23 do not thus appear to be as critical as what
742 can been achieved using the 23 sites of ICOS23. The changes from ICOS23 to ICOS50
743 significantly enhance the uncertainty reduction at 0.5° resolution even in Western Europe in July,
744 e.g., with uncertainty reduction increased from ~40% using ICOS23 to ~60% using ICOS66 in
745 Switzerland. The impact of adding new sites is larger in December than in July, and,
746 consequently, results for western Germany and Benelux converge between July and December
747 when increasing the network to ICOS66.

748 The impact on the scores of uncertainty reduction of the increase of the ICOS network is also
749 significant at the national (compare Fig. 4 and Fig. 8) and European scales (see Table 1 and Fig.
750 9) when comparing results with ICOS50 or ICOS66 to those obtained with ICOS23. The
751 ICOS66 network delivers uncertainty reductions as high as 80% for countries like France and
752 Germany in July. For Europe, the uncertainty reduction when using ICOS66 reaches 79% down
753 to ~15 $TgCmonth^{-1}$ posterior uncertainty in December, and 64% down to ~33 $TgCmonth^{-1}$
754 posterior uncertainty in July. However, the increase from ICOS50 to ICOS66 does not seem to
755 impact much the uncertainty reduction at these scales, especially in July.

756 Figure 9 illustrates the diversity (depending on the space locations) of the evolution of the impact
757 of increasing the network as a function of the NEE averaging spatial scale. For a low altitude site
758 already present in the dense part of ICOS23, the impact of adding new sites increases when
759 increasing the spatial scale of the analysis up to areas where ICOS23 is less dense (mainly in
760 Eastern Europe) and where new sites are included in ICOS50. The impact also increases for
761 SW1 (which is located in the northeastern border of the domain) with increasing spatial
762 aggregation scale since encompassing more and more of the new sites from ICOS23 to ICOS50
763 when extending the averaging domain to the European western area. Conversely, the impact of
764 the addition of new sites can decrease when increasing the NEE spatial aggregation scale, e.g., at
765 HYY where a new site is specifically added in ICOS50.

Deleted: Still, the

Deleted: quite

Deleted: But on the opposite

3.3 Sensitivity to the correlation length of the prior uncertainty

The impact of reducing the correlation e-folding length (from 250 km to 150 km) of the prior uncertainty in the inversion configuration is tested using ICOS66 in July (compare Figs. 7b and 10a, Figs. 8b and 11a, and the corresponding curves in Fig. 9). Such a change of correlation length strongly decreases the values of uncertainty reduction at all spatial scales. This is because it decreases the prior uncertainty at every scale while decreasing the ability of the inversion system to extrapolate in space the information from measurement sites based on the knowledge about spatial correlations of the prior uncertainties. At 0.5° resolution, the areas of high uncertainty reduction narrow around the measurement sites and the smaller overlap of the areas of influence of these sites limits the highest local values of uncertainty reduction to 40%-50% while typical values in Western Europe now range from 20% to 40% instead of 30% to 65% when using $\mathbf{B}_{250}$ (see Sect. 2.2.2 for the definition of the **B** matrices). The uncertainty reduction for countries such as the UK, Germany and Spain decreases when the e-folding correlation length is lowered from 250 km to 150 km, from more than 75%-80% to less than 70%. For the full European domain, it decreases from 64% to 47%.

Even though these decreases can be very large, it is critical to keep in mind that they refer to uncertainty reductions compared to a prior uncertainty which is decreased by the new configuration of **B** (as illustrated at the country scale in Fig. A1). The posterior uncertainty in the European and two-week mean NEE in July using ICOS66 is decreased from ~33 TgC month^{-1} to 29 TgCmonth^{-1} when changing the configuration of **B** from $\mathbf{B}_{250}$ to $\mathbf{B}_{150}$ (Table 1). Similarly, the posterior uncertainty is generally smaller at the national scale when changing the configuration of **B** from $\mathbf{B}_{250}$ to $\mathbf{B}_{150}$ (Fig. A2). We thus have an expected situation for which improving the knowledge on the prior NEE improves that of the posterior NEE even if in our case, the improvement of the knowledge on the prior NEE which is tested here also decreases the ability

Deleted: Fig

Deleted: Fig

Deleted: narrows

to extrapolate in space the information from the atmospheric measurements. However, of note is that when changing the configuration of **B** from $\mathbf{B}_{250}$ to $\mathbf{B}_{150}$, i.e., when changing the spatial correlations between prior uncertainties at 0.5° resolution, but not the standard deviations of the prior uncertainties at 0.5° resolution, we do not improve the knowledge on the prior NEE at the model grid 0.5° resolution. Given the lower uncertainty reduction when using $\mathbf{B}_{150}$, the posterior uncertainties are higher at 0.5° resolution when changing the configuration of **B** from $\mathbf{B}_{250}$ to $\mathbf{B}_{150}$ (Fig. A3).

Deleted: (since modifying the correlations but not the standard deviations in **B**).

3.4 Sensitivity to the observation error

The impact of dividing the standard deviation of the observation error by two in the inversion configuration is tested using ICOS50 in July (compare Figs. 7a and 10b, Figs. 8a and 11b and the corresponding curves in Fig. 9). The decrease of observation error increases the weight of the measurements in the inversion and the resulting uncertainty reduction. This increase is visible at all spatial scales for the aggregation of the NEE, and relatively constant as a function of these spatial scales except at the European scale for which it is smaller, from 64% to 67%. This provides the highest scores of uncertainty reduction of this study at any spatial scales, the impact of division of the observation error by two being larger than that of increasing the ICOS network configuration from ICOS50 to ICOS66.

Deleted: Fig

Deleted: Fig

Deleted: quite

4 Synthesis and conclusions

We assessed the potential of CO_2 mole fraction measurements from three configurations of the ICOS atmospheric network to reduce uncertainties in two-week mean European NEE at various spatial scales in summer and in winter. This assessment is based on a regional variational inverse modeling system with parameters consistent with the knowledge on uncertainties in prior

estimates of NEE from ecosystem models and in atmospheric transport models. The results obtained with the various experiments from this study indicate an uncertainty reduction which ranges between ~50% and 80% for the full European domain, between ~70% and 90% for large countries in Western Europe (such as France, Germany, Spain, UK), where the ICOS network is denser, but below 50% in much cases for eastern countries where there are few ICOS sites even with the ICOS66 configuration. At 0.5° resolution, excluding results when using $\mathbf{B}_{150}$ (for which the uncertainty reduction is applied to a different prior uncertainty), uncertainty reductions range from 30% to 65% in the dense parts of the networks (between northern Spain and eastern Germany) while it is generally below 30% east of Germany and Italy when using ICOS23 or east of Poland and Hungary when using ICOS66. The very high values of uncertainty reduction obtained in areas where ICOS sites are distant by less than the typical length scale of the prior uncertainty (Western Europe when using ICOS23 and a larger area when using ICOS66) is highly promising for the precision of the monitoring of the NEE in these areas in the near term.

Despite the absence of seasonal variation for the uncertainty in the average NEE over Western Europe (at least according to our results for the year 2007) significant seasonal variations at higher resolution or for the full European domain reveal the influence of the atmospheric transport on the scores of uncertainty reduction. Using ICOS66 instead of ICOS23 does not limit this behavior since few sites are added between ICOS23 and ICOS66 in Eastern Europe where the largest seasonal variations of the uncertainty reduction occur. The larger wind speed in December than in July explains that there is a similar uncertainty reduction in July and December for Western Europe. This is another illustration of the influence of the atmospheric transport on the scores of uncertainty reduction. It demonstrates that such scores and their sensitivity to the network extension can hardly be anticipated based on a simple analysis of the site locations and on the knowledge of the typical spatial scale of a station footprint. Their derivation requires such the complex application of an inversion system as in this study.

Deleted: are

Deleted: if

Deleted: impact of the

Deleted: yielding

Deleted: also highlights

Deleted: are not fully intuitive

Deleted: that their

Deleted: a

These scores of uncertainty reduction result in posterior uncertainties lower than 1.8 gC m^{-2} day^{-1} at 0.5° resolution in the areas where the ICOS network is dense. At the national scale, posterior uncertainties scales are compared to the typical estimates of the NEE from the ORCHIDEE model for the corresponding two-week period in July 2007 in Table A2. The relative posterior uncertainty could be less than 20% for the countries having the largest NEE such as France, Germany, Poland or UK (if using ICOS66 in the three last cases, otherwise it should be less than 30% if using ICOS23), even though it would not be the case for Scandinavian countries with a high NEE. For some Eastern European countries, the posterior uncertainty could be very close to the estimate of NEE from ORCHIDEE but the general tendency is to obtain posterior uncertainties much lower than the estimate of the NEE from ORCHIDEE even when using ICOS23. This tendency is reflected at the European scale (Table 1) for which the posterior uncertainty when using ICOS23 and the reference inversion configuration is ~20% and ~30% of the total NEE from ORCHIDEE in July and December respectively. These numbers can be compared to the uncertainty targets defined for the CarbonSat satellite mission (ESA, 2015; of note is that the mission has not been selected for the Earth Explorer 8 opportunity): 0.5 gC m^{-2} day^{-1} at the 500 km ×500 km and 1 month scale. Figures 12, A1 and A2 show that at the 2-week and national scale, the prior uncertainties are systematically larger than this target, but that the posterior uncertainties in Western and Northern Europe are generally close or smaller than this target even when using ICOS23. Since the temporal correlations in the prior uncertainty have a 1 month timescale and since the temporal correlations in the posterior uncertainty should be smaller than that in the prior uncertainty, these uncertainties at the 2-week scale can be considered to be equal or lower than the corresponding uncertainties at the 1 month scale. Therefore, Figures 12, A1 and A2 indicate that the inversion is required to reach the target from the CarbonSat report for mission selection. They also indicate that this target is likely not reached in a large part of South Eastern Europe even when using ICOS66 but that for countries like the Czech Republic and Poland, extending the network from ICOS23 to ICOS66 allows

Deleted: gathering

Deleted: too

Deleted: shows

Deleted: well

Deleted: this indicates

Deleted: It

Deleted: indicates

reaching it. Finally, these figures indicate that the ICOS23 network is sufficient to reach this target in Western Europe.

The comparison of the sensitivity of the results in July to changes in the observation network, correlation lengths of the prior uncertainty and observation error (in the range of tests conducted in this study) indicates a hierarchy of the impact of such changes depending on the spatial scales. Increasing the network from ICOS23 to ICOS50 yields the largest change in posterior uncertainty due to a significantly better monitoring of the eastern part of Europe. However, for western countries, at the grid to national scales, the impact of changing the inversion parameters is generally larger than that of the increase of the network size. Given the range of spatial correlations in the prior uncertainty that are investigated here, the spacing of ICOS sites in Western Europe is already sufficiently narrow to ensure that this full domain is significantly constrained by the measurements from ICOS23. The weight of this constraint at grid to national scales in Western Europe is more directly modified by dividing by two the observation errors or shortening by nearly half the correlation length of the prior uncertainties than by doubling the number of monitoring sites.

The increase of the ICOS network from ICOS23 to ICOS50 or to ICOS66 follow two strategies: a densification of the network in the West and it extension in the poorly monitored area, mainly in the East. The results of this study indicate that the extension should presently focus in the East since notional targets for the posterior uncertainty in national scale NEE (derived from the CarbonSat report for mission selection) are reached in Western Europe when using ICOS23, since the posterior uncertainties from the national scale to the 0.5° scale in Western Europe are weakly sensitive to the increase of the network, and since the results in Eastern Europe are highly sensitive to the increase of the network. These results also raise optimism regarding the increase of the precision in the inverted NEE from improvements of the atmospheric transport

Deleted: it indicated

Deleted: different

Deleted: fact,

Deleted: Western Europe, that

Deleted: are already

Deleted: that the sensitivity of

Deleted: at

Deleted: in

Deleted: is relatively low

Deleted: fact that

Deleted: impacted by the increase of the network encourage a spread of the ICOS network to poorly monitored areas rather than a densification of the core

Deleted: this

Deleted: in Western Europe. This recommendation sounds natural but this study would have rather supported a densification of the network in Western Europe if revealing that the density of the ICOS23 network was not high enough there, so that spreading the network in the East would have resulted in preventing from getting useful information about the NEE anywhere in Europe.

Deleted: benefits

943 modeling or from the improvement of the prior “bottom-up” (as opposed to the “top-down”
944 information from atmospheric concentrations) knowledge on the fluxes.

945 Some limitations of the calculations in this paper should be kept in mind when analyzing the
946 results more precisely. The convergence of the calculations as a function of the number of
947 minimization iterations during the inversion or as a function of the number of inversions in each
948 Monte Carlo ensemble experiment, has been assessed based on average diagnostics. Locally,
949 some results have not converged. Additionally, the use of ICOS50 or ICOS66 should require
950 more minimization iterations to converge to the same extent as when using ICOS23 or ICOS50
951 due to the increase of the dimension of the inversion problem. As an example, this results in the
952 diagnostic of very slight increases (which do not yield significant relative differences) of the
953 posterior uncertainty for Sweden or for Europe when extending ICOS50 to ICOS66. This
954 problem of convergence slightly alter the scores of uncertainty reduction for specific areas only,
955 but it is not significant enough to impact the typical range of values analyzed and the subsequent
956 conclusions in this study.

957 Another point to note is that the confidence in the reference configuration of the inversion has
958 been built based on the diagnostics of the errors in NEE simulated with the ORCHIDEE model
959 at the local scale from Chevallier et al. (2012) and at the monthly and Europe wide scale from
960 Broquet et al. (2013). A simple model is used to represent the correlations of the prior
961 uncertainty in NEE and thus the prior uncertainty in NEE at the intermediate scales. The
962 modeling of the prior uncertainties may need to be refined to better account for the heterogeneity
963 of the European ecosystems with potential impact on the results of posterior uncertainty at fine
964 scales. Furthermore, the assumption that the uncertainties in CO_2 anthropogenic emissions do not
965 have a significant signature at the ICOS sites is based on studies at relatively few monitoring
966 sites corresponding to the coarse atmospheric network of the CarbonEurope-IP project (Schulze
967 et al. 2010). When considering far denser networks with many sites close to urban areas (such as

Deleted: (respectively)

Deleted: of

Deleted: Such problems seem very minor. They

Deleted: they are

Deleted: It

in and around the Netherlands when using ICOS66), this uncertainty should be accounted for. The assumption that uncertainties in the boundary conditions and in the anthropogenic emissions have a weak impact on the inversion is also supported by the results of Broquet et al. (2013) at the European scale only. But when assessing results for specific areas in highly industrialized countries or close to the model domain boundaries such as in this study, the impact of such uncertainties may be larger than when analyzing results at the European scale. Such considerations should lead to further investigation regarding the inversion configuration and thus potential refinement of the results.

This study focuses on results for two-week mean fluxes while a critical target of the inversion should be related to annual mean fluxes. This and the strong influence of the variations of the meteorological conditions on the inversion results (which limits the ability to extrapolate the results to the annual scale) encourage the set-up of 1-year long experiments. However, this study already gives qualitative insights on such results and on their sensitivity to the observing network or to accuracy of the different components of the system which should support future network design studies in Europe. By demonstrating the capability for deriving scores of uncertainty reductions for NEE at 6-hour and 0.5° resolution, it supports the development of operational inversion systems deriving the optimal location for new sites to be installed in the European network.

Deleted: likely

Deleted: on average

Deleted:).

Deleted: such as in this study, this assumption may be weakened

Acknowledgement

This study was co-funded by the European Commission under the EU Seventh Research Framework Programme (grant agreement No. 283080, Geocarbon project) and under the framework of the preparatory phase of ICOS. It was also co-funded by the industrial chair BridGES (supported by the Université de Versailles Saint-Quentin-en-Yvelines, the Commissariat à l'Energie Atomique et aux Energies Renouvelables, the Centre National de la Recherche Scientifique, Thales Alenia Space and Veolia). We also would like to thank the partners of the ICOS infrastructure for providing a list of potential locations for future ICOS atmospheric sites.

Deleted: chaire

References

Ahmadov, R., Gerbig, C., Kretschmer, R., Körner, S., Rödenbeck, C., Bousquet, P., and Ramonet, M.: Comparing high resolution WRF-VPRM simulations and two global CO_2 transport models with coastal tower measurements of CO_2, Biogeosciences, 6, 807-817, doi:10.5194/bg-6-807-2009, 2009.

Bocquet, M.: Grid resolution dependence in the reconstruction of an atmospheric tracer source, Nonlin. Processes Geophys., 12, 219–234, 2005.

Bousserez, N., Henze, D. K., Perkins, A., Bowman, K. W., Lee, M., Liu, J., Deng, F., and Jones, D. B. A.: Improved analysis-error covariance matrix for high-dimensional variational inversions: application to source estimation using a 3-D atmospheric transport model, Q. J. Roy. Meteor. Soc., doi:10.1002/qj.2495, 19021, 19023, 2015.

Bréon, F. M., Broquet, G., Puygrenier, V., Chevallier, F., Xueref-Rémy, I., Ramonet, M., Dieudonné, E., Lopez, M., Schmidt, M., Perrussel, O., and Ciais, P.: An attempt at estimating Paris area CO_2 emissions from atmospheric concentration measurements, Atmos. Chem. Phys. 15, 1707-1724, doi:10.5194/acp-15-1707-2015, 2015.

Broquet, G., Chevallier, F., Rayner, P. J., Aulagnier, C., Pison, I., Ramonet, M., Schmidt, M.,Vermeulen, A. T., and Ciais, P.: A European summertime CO_2 biogenic flux inversion at mesoscale from continuous in situ mixing ratio measurements, J. Geophys. Res., 116, D23303, doi:10.1029/2011JD016202, 2011

Broquet, G., Chevallier, F., Bréon, F.-M., Kadygrov, N., Alemanno, M., Apadula, F., Hammer, S., Haszpra, L., Meinhardt, F., Morguí, J. A., Necki, J., Piacentino, S., Ramonet, M., Schmidt, M., Thompson, R. L., Vermeulen, A. T., Yver, C., and Ciais, P.: Regional inversion of CO_2 ecosystem fluxes from atmospheric measurements: reliability of the uncertainty estimates, Atmos. Chem. Phys., 13, 9039-9056, doi:10.5194/acp-13-9039-2013, 2013.

Chevallier, F., Bréon, F. M., and Rayner, P.J.,: Contribution of the Orbiting Carbon Observatory to the estimation of CO_2 sources and sinks: Theoretical study in a variational data assimilation framework, J. Geophys. Res., 112, D09307, doi:10.1029/2006JD007375, 2007.

Chevallier, F., Wang, T., Ciais, P., Maignan, F., Bocquet, M., Arain A., Cescatti, A., Chen, J., Dolman, A. J., Law, B. E., Margo-lis, H., Montagnani, L., and Moors, E.: What eddy-covariance measurements tell us about prior land flux errors in CO_2-flux inversion schemes, Global Biogeochem. Cycles, 26, GB1021, doi:10.1029/2010GB003974, 2012.

Ciais, P., Dolman, A. J., Bombelli, A., Duren, R., Peregon, A., Rayner, P. J., Miller, C., Gobron, N., Kinderman, G., Marland, G., Gruber, N., Chevallier, F., Andres, R. J., Balsamo, G., Bopp, L., Bréon, F.-M., Broquet, G., Dargaville, R., Battin, T. J., Borges, A., Bovensmann, H., Buchwitz, M., Butler, J., Canadell, J. G., Cook, R. B., DeFries, R., Engelen, R., Gurney, K. R., Heinze, C., Heimann, M., Held, A., Henry, M., Law, B., Luyssaert, S., Miller, J., Moriyama, T., Moulin, C., Myneni, R. B., Nussli, C., Obersteiner, M., Ojima, D., Pan, Y., Paris, J.-D., Piao, S. L., Poulter, B., Plummer, S., Quegan, S., Raymond, P., Reichstein, M., Rivier, L., Sabine, C., Schimel, D., Tarasova, O., Valentini, R., Wang, R., van der Werf, G., Wickland, D., Williams, M., and Zehner, C.: Current systematic carbon-cycle observations and the need for

implementing a policy-relevant carbon observing system, Biogeosciences, 11, 3547-3602, doi:10.5194/bg-11-3547-2014, 2014.

Claeyman, M., Attié, J.-L., Peuch, V.-H., El Amraoui, L., Lahoz, W. A., Josse, B., Joly, M., Barré, J., Ricaud, P., Massart, S., Piacentini, A., von Clarmann, T., Höpfner, M., Orphal, J., Flaud, J.-M. and Edwards, D. P.: A thermal infrared instrument onboard a geostationary platform for CO and O3 measurements in the lowermost troposphere: Observing System Simulation Experiments (OSSE), Atmos. Meas. Tech., 4, 1637-1661, doi:10.5194/amt-4-1637-2011, 2011.

Edwards, D. P., Arellano Jr., A. F. and Deeter M. N.: A satellite observation system simulation experiment for carbon monoxide in the lowermost troposphere, J. Geophys. Res., 114, D14304, doi:10.1029/2008JD011375, 2009.

Enting, I. G.: Inverse Problems in Atmospheric Constituent Transport, Cambridge Univ. Press, Cambridge, U. K., 2002.

Errico, R. M., Yang, R., Privé, N. C., Tai, K.-S., Todling, R., Sienkiewicz, M. E. and Guo, J.: Development and validation of observing-system simulation experiments at NASA's Global Modeling and Assimilation Office. Q.J.R. Meteorol. Soc., 139: 1162–1178,doi: 10.1002/qj.2027, 2013.

ESA, Report for Mission Selection: CarbonSat, ESA SP-1330/1, (2 volume series), European Space Agency, Noordwijk, The Netherlands, 2015.

Francey, R.J. (Ed.): Report of the Ninth WMO meeting of experts on carbon dioxide concentration and related tracer measurement techniques. Aspendale, Vic., Australia, 1–4 September 1997, World Meteorological Organization (WMO), Geneva, Series: Global Atmosphere Watch (GAW); no. 132; WMO; TD no. 952, 132 pp., 1998.

Gerbig, C., Lin, J. C., Munger, J. W., and Wofsy, S. C.: What can tracer observations in the continental boundary layer tell us about surface-atmosphere fluxes?, Atmos. Chem. Phys., 6, 539-554, doi:10.5194/acp-6-539-2006, 2006.

Gilbert, J. C., and Lemaréchal, C.,: Some numerical experiments with variable-storage quasi-Newton algorithms, Math. Program., 45, 407–435, 1989.

Göckede, M., Turner, D. P., Michalak, A. M., Vickers, D. and Law B. E.: Sensitivity of a subregional scale atmospheric inverse CO_2 modeling framework to boundary conditions, J. Geophys. Res., 115, D24112, doi:10.1029/2010JD014443, 2010.

Gurney, K. R., Law, R. M., Denning, A. S., Rayner, P. J., Baker, D., Bousquet, P., Bruhwiler, L., Chen, Y.-H., Ciais, P., Fan, S., Fung, I. Y., Gloor, M., Heimann, M., Higuchi, K., John, J., Maki, T., Maksyutov, S., Masarie, K., Peylin, P., Prather, M., Pak, B. C., Randerson, J., Sarmiento, J., Taguchi, S., Takahashi, T., and Yuen, C.-W.: Towards robust regional estimates of CO_2 sources and sinks using atmospheric transport models, Nature, 415, 626–630, 2002.

Halliwell Jr., G. R., Srinivasan, A., Kourafalou, V., Yang, H., Willey, D., Le Hénaff, M. and Atlas, R.: Rigorous Evaluation of a Fraternal Twin Ocean OSSE System for the Open Gulf of Mexico. J. Atmos. Oceanic Technol., **31**, 105–130, doi: 10.1175/JTECH-D-13-00011.1, 2014.

Hourdin, F., Musat I., Bony S., Braconnot P., Codron F., Dufresne J. L., Fairhead L., Filiberti M. A., Friedlingstein P., Grandpeix J. Y., Krinner G., LeVan P., Li Z.X., Lott F.: The LMDZ4 general circulation model: Climate performance and sensitivity to parametrized physics with emphasis on tropical convection, J. Clim. Dyn., 27, 787–813, doi:10.1007/s00382-006- 0158-0, 2006.

Houweling, S., Breon, F.-M., Aben, I., Rödenbeck, C., Gloor, M., Heimann, M., and Ciais, P.: Inverse modeling of CO_2 sources and sinks using satellite data: a synthetic inter-comparison of measurement techniques and their performance as a function of space and time, Atmos. Chem. Phys., 4, 523-538, doi:10.5194/acp-4-523-2004, 2004.

Hungershoefer, K., Breon, F.-M., Peylin, P., Chevallier, F., Rayner, P., Klonecki, A., Houweling, S., and Marshall, J.: Evaluation of various observing systems for the global monitoring of CO_2 surface fluxes, Atmos. Chem. Phys., 10, 10503-10520, doi:10.5194/acp-10-10503-2010, 2010.

Kadygrov, N., Maksyutov, S., Eguchi, N., Aoki, T., Nakazawa, T., Yokota, T., and Inoue, G.: Role of simulated GOSAT total column CO_2 observations in surface CO_2 flux uncertainty reduction, J. Geophys. Res., 114, D21208, doi:10.1029/2008JD011597, 2009.

Krinner, G., Viovy, N., de Noblet-Ducoudré, N., Ogée, J., Polcher, J., Friedlingstein, P., Ciais, P., Sitch, S., and Prentice, I. C.: A dynamic global vegetation model for studies of the coupled atmospherebiosphere system, Global Biogeochem. Cycles, 19, GB1015, doi:10.1029/2003GB002199, 2005.

Lauvaux, T., Uliasz, M., Sarrat, C., Chevallier, F., Bousquet, P., Lac, C., Davis, K. J., Ciais, P., Denning, A. S., and Rayner, P. J.: Mesoscale inversion: first results from the CERES campaign with synthetic data, Atmos. Chem. Phys., 8, 3459–3471, doi:10.5194/acp-8-3459-2008, 2008.

Lauvaux, T., Schuh, A. E., Uliasz, M., Richardson, S., Miles, N., Andrews, A. E., Sweeney, C., Diaz, L. I., Martins, D., Shepson, P. B., and Davis, K. J.: Constraining the CO_2 budget of the corn belt: exploring uncertainties from the assumptions in a mesoscale inverse system, Atmos. Chem. Phys., 12, 337-354, doi:10.5194/acp-12-337-2012, 2012.

Law, R. M., Peters, W., Roedenbeck, C., Aulagnier, C., Baker, I., Bergmann, D. J., Bousquet, P., Brandt, J., Bruhwiler, L., Cameron-Smith, P. J., Christensen, J. H., Delage, F., Den-ning, A. S., Fan, S., Geels, C., Houweling, S., Imasu, R., Karstens, U., Kawa, S. R., Kleist, J., Krol, M. C., Lin, S. J., Lokupitiya, R., Maki, T., Maksyutov, S., Niwa, Y., Onishi, R., Parazoo, N., Patra, P. K., Pieterse, G., Rivier, L., Satoh, M., Serrar, S., Taguchi, S., Takigawa, M., Vautard, R., Ver-meulen, A. T., and Zhu, Z.: TransCom model simulations of hourly atmospheric CO_2: Experimental overview and diurnal cycle results for 2002, Global Biogeochem. Cycles., 22, GB3009, doi:10.1029/2007gb003050, 2008.

Marécal, V., Peuch, V.-H., Andersson, C., Andersson, S., Arteta, J., Beekmann, M., Benedictow, A., Bergström, R., Bessagnet, B., Cansado, A., Chéroux, F., Colette, A., Coman, A., Curier, R. L., Denier van der Gon, H. A. C., Drouin, A., Elbern, H., Emili, E., Engelen, R. J., Eskes, H. J., Foret, G., Friese, E., Gauss, M., Giannaros, C., Guth, J., Joly, M., Jaumouillé, E., Josse, B., Kadygrov, N., Kaiser, J. W., Krajsek, K., Kuenen, J., Kumar, U., Liora, N., Lopez, E., Malherbe,

L., Martinez, I., Melas, D., Meleux, F., Menut, L., Moinat, P., Morales, T., Parmentier, J., Piacentini, A., Plu, M., Poupkou, A., Queguiner, S., Robertson, L., Rouïl, L., Schaap, M., Segers, A., Sofiev, M., Tarasson, L., Thomas, M., Timmermans, R., Valdebenito, Á., van Velthoven, P., van Versendaal, R., Vira, J., and Ung, A.: A regional air quality forecasting system over Europe: the MACC-II daily ensemble production, Geosci. Model Dev., 8, 2777-2813, doi:10.5194/gmd-8-2777-2015, 2015.

Masutani, M., Schlatter, T. W., Errico, R. M., Stoffelen, A., Andersson, E., Lahoz, W., Woollen, J. S., Emmitt, G. D., Riishøjgaard, L.-P. and Lord, S. J.: "Observing System Simulation Experiments" in Data Assimilation: Making sense of observations, Eds. Lahoz, W. A., Khattatov B. and Ménard, R., Springer, Berlin, pp 647-679, 2010.

Meesters, A. G. C. A., Tolk, L.F., Peters, W., Hutjes, R. W. A., Velinga, O.S., Elbers, J.A., Vermeulen, A.T., van der Laan, S., Neubert, R. E. M., Meijer, H. A. J. and Dolman, A. J.: Inverse carbon dioxide flux estimates for the Netherlands, J. Geophys. Res.,117, D20306, doi:10.1029/2012JD017797, 2012.

Peters, W., Krol, M. C., Van Der Werf, G. R., Houweling, S., Jones, C. D., Hughes, J., Schaefer, K., Masarie, K. A., Jacobson, A. R., Miller, J. B., Cho, C. H., Ramonet, M., Schmidt, M., Ciattaglia, L., Apadula, F., Heltai, D., Meinhardt, F., Di Sarra, A. G., Piacentino, S., Sferlazzo, D., Aalto, T., Hatakka, J., Strom, J., Haszpra, L., Meijer, H. A. J., Van Der Laanm, S., Neubert, R. E. M., Jordan, A., Rodo, X., Morgui, J.-A., Vermeulen, A. T., Popa, E., Rozanski, K., Zimnoch, M., Manning, A. C., Leuenberger, M., Uglietti, C., Dolman, A. J., Ciais, P., Heimann, M. and Tans, P. P.: Seven years of recent European net terrestrial carbon dioxide exchange constrained by atmospheric observations. Global Change Biology, 16: 1317–1337. doi: 10.1111/j.1365-2486.2009.02078.x, 2010.

Peylin, P., Houweling, S., Krol, M. C., Karstens, U., Rödenbeck, C., Geels, C., Vermeulen, A., Badawy, B., Aulagnier, C., Pregger, T., Delage, F., Pieterse, G., Ciais, P., and Heimann, M.: Importance of fossil fuel emission uncertainties over Europe for CO_2 modeling: model intercomparison, Atmos. Chem. Phys., 11, 6607-6622, doi:10.5194/acp-11-6607-2011, 2011.

Peylin, P., Law, R. M., Gurney, K. R., Chevallier, F., Jacobson, A. R., Maki, T., Niwa, Y., Patra, P. K., Peters, W., Rayner, P. J., Roedenbeck, C., van der Laan-Luijkx, I. T., and Zhang, X.: Global atmospheric carbon budget: results from an ensemble of atmospheric CO_2 inversions, Biogeosciences, 10, 6699-6720, doi:10.5194/bg-10-6699-2013, 2013.

Rayner, P. J., Enting, I.G., and Trudinger, C. M.,: Optimizing the CO_2 observing network for constraining sources and sinks, Tellus B, 48(4), 433-444, 1996.

Riishøjgaard, L. P., Ma, Z., Masutani, M., Woollen, J. S., Emmitt, G. D., Wood, S. A. and Greco, S.: Observation system simulation experiments for a global wind observing sounder, Geophys. Res. Lett., 39, L17805, doi:10.1029/2012GL051814, 2012.

Roedenbeck, C., Houweling, S., Gloor, M., and Heimann, M.: CO_2 flux history 1982–2001 inferred from atmospheric data using a global inversion of atmospheric transport, Atmos. Chem. Phys., 3, 1919-1964, doi:10.5194/acp-3-1919-2003, 2003.

Schmidt, H., Derognat, C., Vautard, R., and Beekmann, M.:A comparison of simulated and observed ozone mixing ratios for the summer of 1998 in Western Europe, Atmos. Environ., 35(36), 6277–6297, doi:10.1016/S1352-2310(01)00451-4, 2001.

Deleted: Riishojgaard

Schuh, A. E., Denning, A. S., Corbin, K. D., Baker, I. T., Uliasz, M., Parazoo, N., Andrews, A. E., and Worthy, D. E. J.: A regional high-resolution carbon flux inversion of North America for 2004. Biogeosciences 7, 1625–1644, doi: 10.5194/bg-7-1625-2010, 2010.

Schulze, E. D., Ciais, P., Luyssaert, S., Schrumpf, M., Janssens, I. A., Thiruchittampalam, B., Theloke, J., Saurat, M., Bringezu, S., Lelieveld, J., Lohila, A., Rebmann, C., Jung, M., Bastviken, D., Abril, G., Grassi, G., Leip, A., Freibauer, A., Kutsch, W., Don, A., Nieschulze, J., Borner, A., Gash, J. H., and Dolman, A. J.: The European carbon balance. Part 4: integration of carbon and other trace-gases fluxes, Global Change Biol., 16, 1451–1469, 2010.

Takahashi, T., Sutherland, S. C. , Wanninkhof, R. , Sweeney, C. , Feely, R. A. , Chipman, D. W. , Hales, B. , Friederich, G. , Chavez, F. , Sabine, C. , Watson, A. , Bakker, D. C. E. , Schuster, U. , Metzl, N. , Yoshikawa-Inoue, H. , Ishii, M. , Midorikawa, T. , Nojiri, Y. , Körtzinger, A. , Steinhoff, T. , Hoppema, M. , Olafsson, J. , Arnarson, T. S. , Tilbrook, B. , Johannessen, T. , Olsen, A. , Bellerby, R., Wong, C. S., Delille, B., Bates, N. R., and de Baar, H. J. W.: Climatological mean and decadal change in surface ocean pCO_2, and net sea-air CO_2 flux over the global oceans , Deep-Sea Research II 56(8-10), pp. 554-577 .doi:10.1016/j.dsr2.2008.12.009, 2009.

Timmermans, R. M. A., Schaap, M., Elbern, H., Siddans, R., Tjemkes. S., Vautard, R. and Builtjes, P.: An Observing System Simulation Experiment (OSSE) for Aerosol Optical Depth from Satellites. J. Atmos. Ocean Tech., **26**, 2673-2682, 2009a.

Timmermans, R. M. A., Segers, A. J., Builtjes, P. J. H., Vautard, R., Siddans, R., Elbern, H., Tjemkes, S. A. T. and Schaap, M.: The added value of a proposed satellite imager for ground level particulate matter analyses and forecasts. IEEE J. Sel. Top. Appl., **2**, 271–283, 2009b.

Timmermans, R.M.A., Lahoz, W.A., Attié, J.-L., Peuch, V.-H., Curier, R.L., Edwards, D.P., Eskes, H.J., Builtjes, P.J.H.: Observing System Simulation Experiments for air quality, Atmospheric Environment doi: 10.1016/j.atmosenv.2015.05.032, 2015.

Tolk, L. F., Dolman, A. J., Meesters, A. G. C. A., and Peters, W.: A comparison of different inverse carbon flux estimation approaches for application on a regional domain, Atmos. Chem. Phys., 11, 10349-10365, doi:10.5194/acp-11-10349-2011, 2011.

Weaver, A.T., Vialard, J., Anderson, D.L.T, Delecluse, P.: Three- and four-dimensional variational assimilation with an ocean general circulation model of the tropical PacificOcean. Part I: formulation, internal diagnostics and consistency checks, Mon. Wea.Rev., 131, 1360-1378, 2003.

World Meteorological Organization: “Scientific Requirements” in Report of the WMO/UNEP/ICSU Meeting on Instruments, Standardization and measurement techniques for atmospheric CO_2, Geneva, Switzerland, 8-11 September 1981.

Zhang, X., Gurney, K. R., Rayner, P., Baker, D., and Liu, Y.-P.: Sensitivity of simulated CO_2 concentration to sub-annual variations in fossil fuel CO_2 emissions, Atmos. Chem. Phys. Discuss., 15, 20679-20708, doi:10.5194/acpd-15-20679-2015, 2015.

Ziehn, T., Nickless, A., Rayner, P. J., Law, R. M., Roff, G., and Fraser, P.: Greenhouse gas network design using backward Lagrangian particle dispersion modelling − Part 1: Methodology and Australian test case, Atmos. Chem. Phys., 14, 9363-9378, doi:10.5194/acp-14-9363-2014, 2014.

Table 1. Uncertainty reduction in two-week and European mean NEE for July and December as a function of the observation network and of the configuration of the inversion parameters ($\mathbf{B}_{250}$ or $\mathbf{B}_{150}$ for $\mathbf{B}$ and $\mathbf{R}_{ref}$ or $\mathbf{R}_{red}$ for $\mathbf{R}$).

	Month	B	R	Prior uncertainty ($TgCmonth^{-1}$)	Posterior uncertainty ($TgCmonth^{-1}$)	NEE from ORCHIDEE ($TgCmonth^{-1}$)	Uncertainty Reduction (%)
ICOS23	July	B_{250}	R_{ref}	91.2	42.6	-201.6	53
	December	B_{250}	R_{ref}	74.9	25.5	80.3	66
ICOS50	July	B_{250}	R_{ref}	91.2	32.4	-201.6	64
	December	B_{250}	R_{ref}	74.9	19.5	80.3	74
	July	B_{250}	R_{red}	91.2	30.4	-201.6	67
ICOS66	July	B_{250}	R_{ref}	91.2	32.8	-201.6	64
	December	B_{250}	R_{ref}	74.9	15.4	80.3	79
	July	B_{150}	R_{ref}	55.0	29.2	-201.6	47

Table A1. Atmospheric measurement sites for the different ICOS network configurations considered in this study with associated observation errors in the reference configuration of the inversion. Two values are given for the observation error at a given site for low altitude sites: that for temporal window 12:00-18:00 (left) and temporal window 18:00-20:00 (right), and one value for temporal window 00:00-06:00 at high altitude sites. Height corresponds to the vertical location of the site above the ground level (magl) and elevation corresponds to its vertical location above sea level (masl).

Deleted: the

Deleted: of the ground

Deleted: at the site position.

Network	Site	Country	Code	type	Lon	Lat	Height magl	Elevation masl	Assim. Window	Obs. Err. (ppm) July	Dec
ICOS23	Bialystok	PL	bik	TT	23.01	53.23	300	480	12-20	4.2-7.2	10.2-15.2
	Biscarrose	FR	bis	G	-1.23	44.38	47	120	12-20	4.2-7.2	10.2-15.2
	Cabauw	NL	cbw	TT	4.93	51.97	200	200	12-20	4.2-7.2	10.2-15.2
	Monte Cimone	IT	cmn	G	10.68	44.17	12	2177	00-06	3.6	3.6
	Gif-sur-Yvette	FR	gif	G	2.15	48.71	7	167	12-20	4.2-7.2	10.2-15.2
	Heidelberg	DE	hei	G	8.67	49.42	30	146	12-20	4.2-7.2	10.2-15.2
	Hegyhatsal	HN	hun	TT	16.65	46.96	115	363	12-20	4.2-7.2	10.2-15.2
	Jungfraujoch	CH	jfj	G	7.98	46.55	gl	3580	00-06	3.6	3.6
	Kasprowy Wierch	PL	kas	G	19.98	49.23	gl	1987	00-06	3.6	3.6
	Lampedusa	IT	lmp	G	12.63	35.52	8	58	12-20	4.2-7.2	10.2-15.2
	La Muela	ES	lmu	TT	-1.1	41.59	79	649	12-20	4.2-7.2	10.2-15.2
	Lutjewad	NL	lut	G	6.35	53.4	60	61	12-20	4.2-7.2	10.2-15.2
	Mace Head	IR	mhd	G	-9.9	53.33	15	40	12-20	4.2-7.2	10.2-15.2
	Ochsenkopf	DE	oxk	TT	11.81	50.03	163	1185	00-06	3.6	3.6
	Pallas	FI	pal	G	24.12	67.97	5	565	12-20	4.2-7.2	10.2-15.2
	Plateau Rosa	IT	prs	G	7.7	45.93	gl	3480	00-06	3.6	3.6
	Puy de Dôme	FR	puy	G	2.97	45.77	10	1475	00-06	3.6	3.6
	Schauinsland	DE	sch	G	7.92	47.9	gl	1205	00-06	3.6	3.6
	Trainou	FR	trn	TT	2.11	47.96	180	311	12-20	4.2-7.2	10.2-15.2
	Westerland	DE	wes	G	8.32	54.93	gl	12	12-20	4.2-7.2	10.2-15.2
	Angus	UK	tta	TT	-2.98	56.56	220	520	12-20	4.2-7.2	10.2-15.2
	Egham	UK	egh	G	-0.55	51.43	5	45	12-20	4.2-7.2	10.2-15.2
	Norunda	SE	nor	TT	17.48	60.09	102	147	12-20	4.2-7.2	10.2-15.2
ICOS50	Kresin u Pacova	CZ	kre	TT	15.08	49.57	250	790	12-20	4.2-7.2	10.2-15.2
	Hohenpeißenberg	DE	hpb	TT	11.01	47.8	159	1106	00-06	3.6	3.6
	Zugspitze	DE	zug	G	10.98	47.42	10	2660	00-06	3.6	3.6
	Risø Meteorological Mast	DK	ris	TT	12.09	55.65	125	130	12-20	4.2-7.2	10.2-15.2
	Høvsøre Wind Test Station	DK	hov	TT	8.15	56.44	116	116	12-20	4.2-7.2	10.2-15.2
	Carnsore Point EMEP monitoring Station	IR	crn	G	-6.33	52.06	3	3	12-20	4.2-7.2	10.2-15.2
	Malin Head Synoptic Meteorological Station	IR	mld	G	-7.37	55.38	3	13	12-20	4.2-7.2	10.2-15.2
	Katowice Kosztowy	PL	kat	TT	19.12	50.19	355	655	12-20	4.2-7.2	10.2-15.2

	Piła Rusionow	PL	pil	TT	16.26	53.17	320	455	12-20	4.2-7.2	10.2-15.2
	Jemiolow	PL	jem	TT	15.28	52.35	314	475	12-20	4.2-7.2	10.2-15.2
	Hyltemossa	SE	hyl	TT	13.42	56.1	150	255	12-20	4.2-7.2	10.2-15.2
	Observatoire Pérenne de l'Environnement	FR	ope	TT	5.36	48.48	120	512	12-20	4.2-7.2	10.2-15.2
	Observatoire de Haute Provence	FR	ohp	TT	5.71	43.93	100	740	12-20	4.2-7.2	10.2-15.2
	Pic du Midi	FR	pdm	G	0.14	42.94	10	2887	00-06	3.6	3.6
	SMEAR II Hyytiälä	FI	hyy	TT	24.29	61.85	127	308	12-20	4.2-7.2	10.2-15.2
	Puijo-Koli	FI	pui	TT	27.65	62.9	176	406	12-20	4.2-7.2	10.2-15.2
	ICOS eastern Finland										
	Utö - Baltic sea	FI	uto	G	21.38	59.78	60	68	12-20	4.2-7.2	10.2-15.2
	Finokalia	GR	fik	G	25.67	35.34	2	152	12-20	4.2-7.2	10.2-15.2
	Birkenes Observatory	NO	bir	G	8.25	58.38	gl	190	12-20	4.2-7.2	10.2-15.2
	Andøya Observatory	NO	and	G	16.01	69.27	gl	380	12-20	4.2-7.2	10.2-15.2
	Svartberget	SE	sva	TT	19.78	64.26	150	385	12-20	4.2-7.2	10.2-15.2
	Tacolneston (norfolk)	UK	tac	G	1.14	52.52	191	261	12-20	4.2-7.2	10.2-15.2
	Ridge Hill	UK	rhi	G	-2.54	52	152	356	12-20	4.2-7.2	10.2-15.2
	Delta Ebre	ES	dec	TT	0.79	40.74	11	16	12-20	4.2-7.2	10.2-15.2
	Valderejo	ES	val	TT	-3.21	42.87	25	1100	00-06	3.6	3.6
	Xures-Invernadeiro	ES	xic	TT	-8.02	41.98	30	902	12-20	4.2-7.2	10.2-15.2
	Ispra	IT	isp	G	8.63	45.81	40	230	12-20	4.2-7.2	10.2-15.2
ICOS66	Lindenberg	DE	lin	TT	14.12	52.21	99	192	12-20	4.2-7.2	10.2-15.2
	Mannheim	DE	man	TT	8.49	49.49	213	323	12-20	4.2-7.2	10.2-15.2
	Gartow 2	DE	grt	TT	11.44	53.07	344	410	12-20	4.2-7.2	10.2-15.2
	Messkirch/Rohrdorf	DE	msr	TT	9.12	48.02	240	892	12-20	4.2-7.2	10.2-15.2
	Wesel	DE	wsl	TT	6.57	51.65	321	340	12-20	4.2-7.2	10.2-15.2
	Helgoland	DE	hlg	G	7.9	54.18	10	40	12-20	4.2-7.2	10.2-15.2
	Iznajar	ES	izn	TT	-4.38	37.28	5	555	12-20	4.2-7.2	10.2-15.2
	Hengelo	NL	hen	G	6.75	52.34	70	80	12-20	4.2-7.2	10.2-15.2
	Goes	NL	goe	G	3.78	51.48	70	70	12-20	4.2-7.2	10.2-15.2
	Peel	NL	pee	G	5.98	51.37	70	80	12-20	4.2-7.2	10.2-15.2
	Noordzee	NL	nse	G	4.73	54.85	50	50	12-20	4.2-7.2	10.2-15.2
	Cap Corse	FR	cor	G	9.35	42.93	35	85	12-20	4.2-7.2	10.2-15.2
	Roc Tredudon	FR	roc	G	-3.91	48.41	10	373	12-20	4.2-7.2	10.2-15.2
	Alfabia	ES	alf	TT	2.72	39.74	gl	1069	00-06	3.6	3.6
	Saissac	FR	sai	TT	2.1	43.39	300	800	00-06	3.6	3.6
	NIO	FR	nio	TT	0.05	46.19	330	503	12-20	4.2-7.2	10.2-15.2

1303

1304

1305

Table A2. NEE uncertainty budget for European countries for July 2007 estimated using the reference inversion configuration and different atmospheric CO_2 networks. Uncertainty reduction values (UR) are shown in the last two columns for ICOS23 and ICOS66.

Country	**NEE**, TgCcountry^{-1}month^{-1}	**NEE prior unc.** TgCcountry^{-1}month^{-1}	**NEE post. Unc.** TgCcountry^{-1}month^{-1}		**UR (%)**	
			ICOS23	**ICOS66**	**ICOS23**	**ICOS66**
Austria	-3.95	4.60	1.49	1.56	**68**	**66**
Belgium	-1.05	1.88	0.69	0.69	**63**	**63**
Bulgaria	-1.22	5.72	5.43	4.06	**5**	**29**
Croatia	-1.64	2.27	1.17	1.13	**48**	**50**
Cyprus	0.04	0.18	0.18	0.18	**0**	**1**
Czech Republic	-4.35	4.08	2.06	1.52	**50**	**63**
Denmark	-1.97	1.74	1.35	0.76	**22**	**57**
Estonia	-2.67	2.37	1.66	1.42	**30**	**40**
Finland	-8.37	11.56	5.92	3.14	**49**	**73**
France	-17.16	18.41	3.52	3.04	**81**	**84**
Germany	-16.00	14.20	4.73	2.73	**67**	**81**
Greece	0.09	3.58	3.45	2.89	**4**	**19**
Hungary	-2.19	4.95	2.61	2.31	**47**	**53**
Ireland	-2.49	2.42	1.68	1.27	**30**	**48**
Italy	-4.44	9.83	4.24	3.82	**57**	**61**
Latvia	-3.61	3.32	2.33	2.22	**30**	**33**
Lithuania	-3.92	3.42	2.02	2.10	**41**	**39**
Luxembourg	-0.12	0.17	0.10	0.10	**42**	**44**
Netherlands	-0.97	1.99	0.65	0.50	**68**	**75**
Norway	-6.02	9.65	4.85	4.65	**50**	**52**
Poland	-21.10	13.26	5.02	4.24	**62**	**68**

Portugal	-1.17	4.24	3.71	2.80	**12**	**34**
Romania	-7.14	10.79	9.14	8.34	**15**	**23**
Slovakia	-2.82	2.59	1.30	1.30	**50**	**50**
Slovenia	-1.17	1.04	0.48	0.43	**54**	**58**
Spain	-3.54	19.90	7.16	3.97	**64**	**80**
Sweden	-9.84	16.50	7.53	5.62	**54**	**66**
Switzerland	-1.72	2.61	1.03	0.68	**60**	**74**
UK	-8.52	7.56	2.11	1.59	**72**	**79**

1309

1310

1311

1312

1313

1314

1315

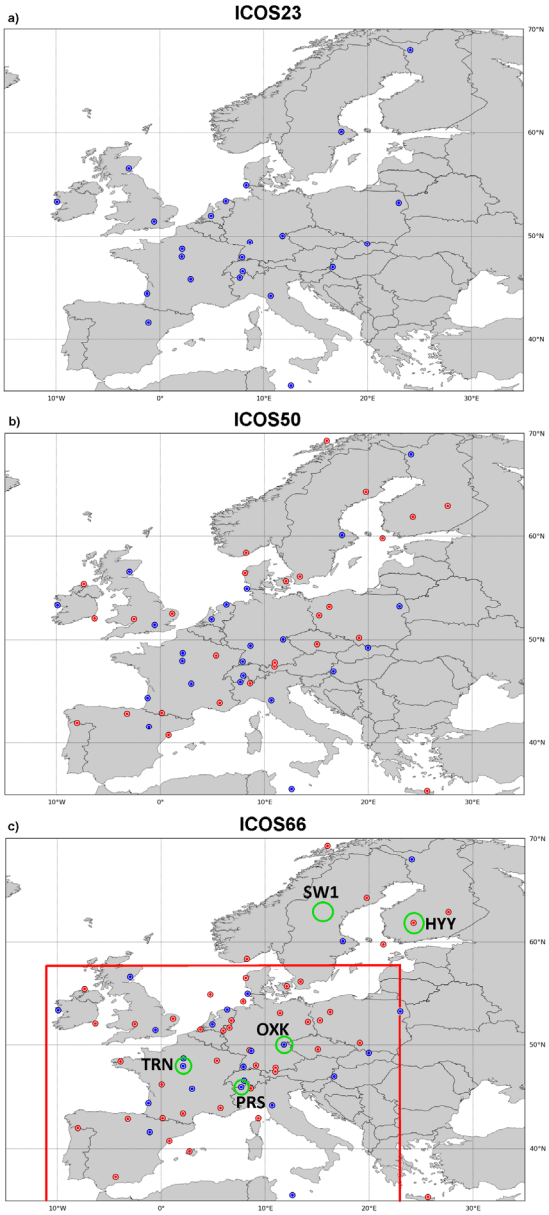

1316

1317 **Figure 1.** Site location for the different ICOS network configurations used in this study: **(a)**

1318 ICOS23 **(b)** ICOS50 **(c)** ICOS66. Dark blue circles correspond to ICOS23 and the red circles are

1319 the new sites for ICOS50 and ICOS66 compared to ICOS23. The European domain (~6.8 * 10^6

1320 km^2 of land surface) covered by these figures corresponds to the domain of the configuration of

1321 the CHIMERE atmospheric transport model used in this study. The red rectangle in (**c**)

corresponds to a western European domain (WE domain, ~3.5 * 10^6 km^2 of land surface) which is used for some of the present analysis because it is significantly better sampled by the ICOS networks than other areas. Green circles in (**c**) are the station locations used for the study of the uncertainty reduction as a function of the spatial scale of the aggregation around each station (in Sect. 3.1.4).

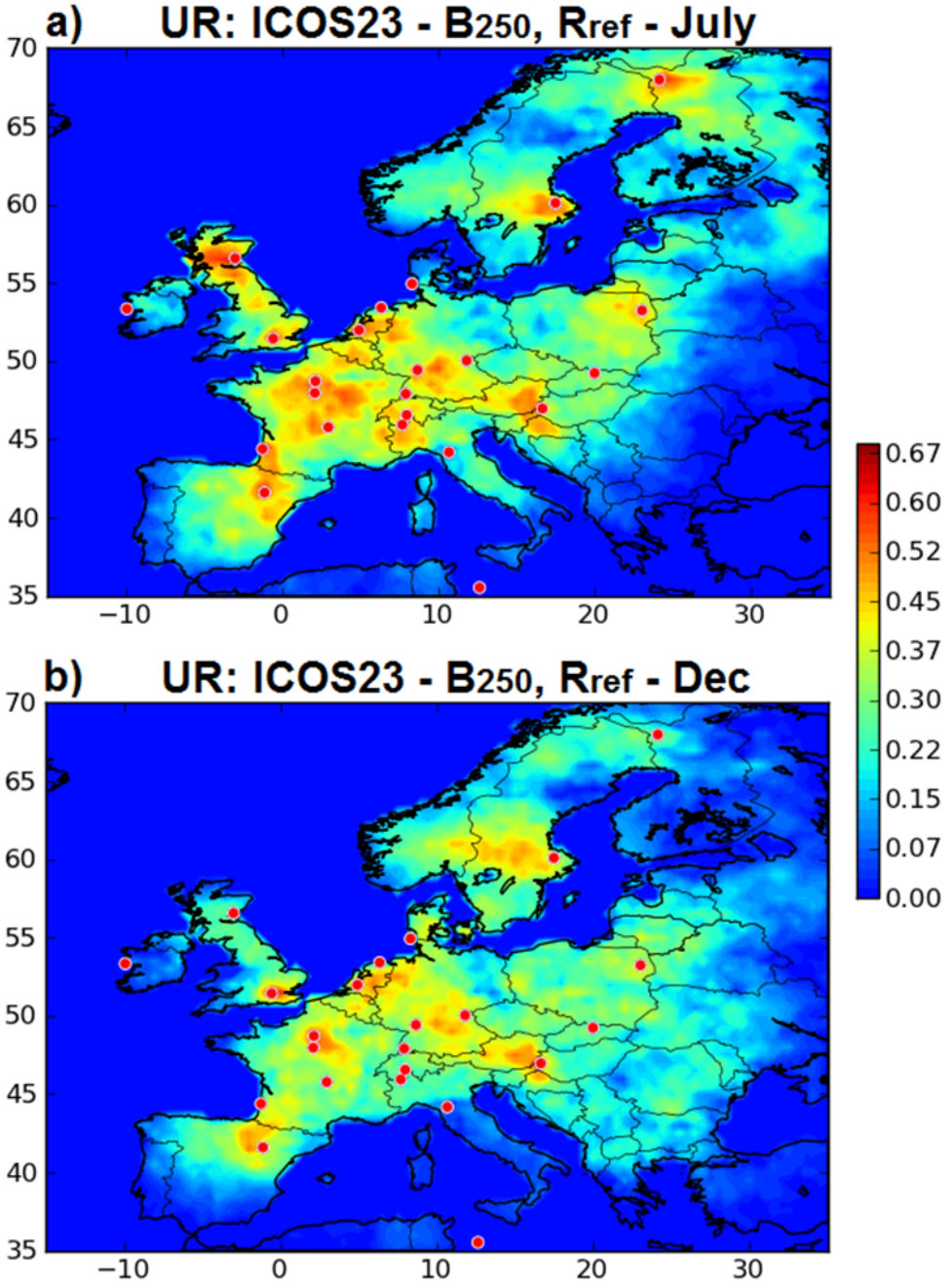

Figure 2. Uncertainty reduction (theoretically comprised between 0 and 1) for two-week mean NEE at 0.5° resolution in July **(a)** and in December **(b)** when using ICOS23 (red dots) and the

reference inversion set-up. Red/blue colors indicate relatively high/low uncertainty reduction (with min = 0, max = 0.68 in the color scale).

Deleted: setup

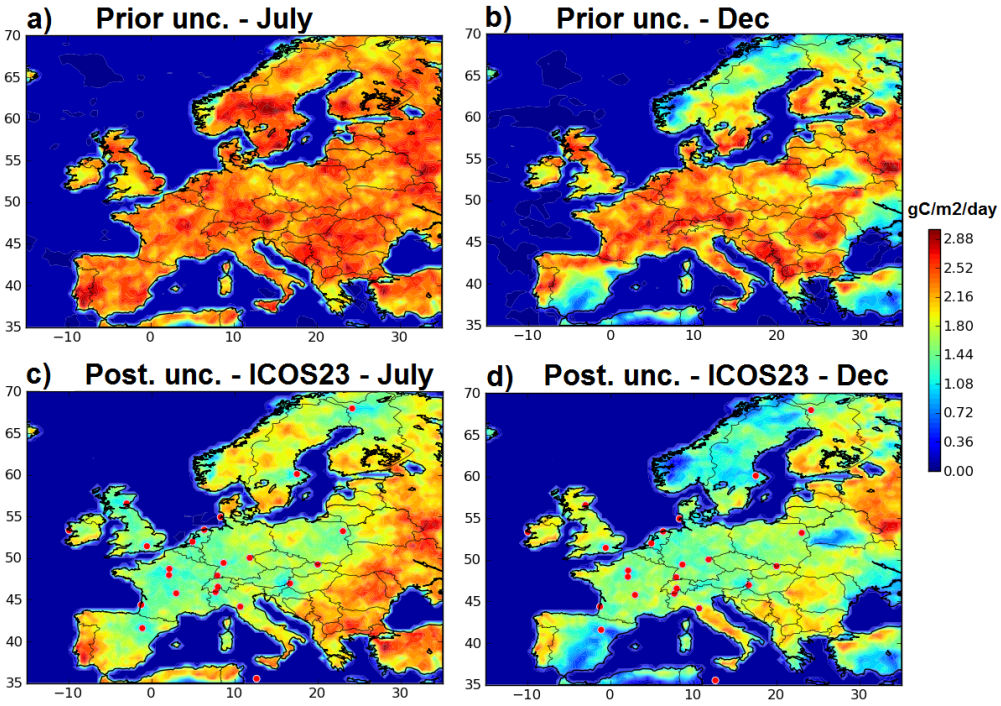

Figure 3. Standard deviations ($gCm^{-2}day^{-1}$) of the prior **(a,b)** and posterior **(c,d)** uncertainties in two-week mean NEE at 0.5° resolution for **(a,c)** July and **(b,d)** December. Posterior uncertainties are given for inversions using ICOS23 (red dots) and the reference inversion set-up. Red/blue colors indicate relatively high/low uncertainties (with min = 0 $gCm^{-2}day^{-1}$, max = 3 $gCm^{-2}day^{-1}$ in the color scale).

Deleted: setup

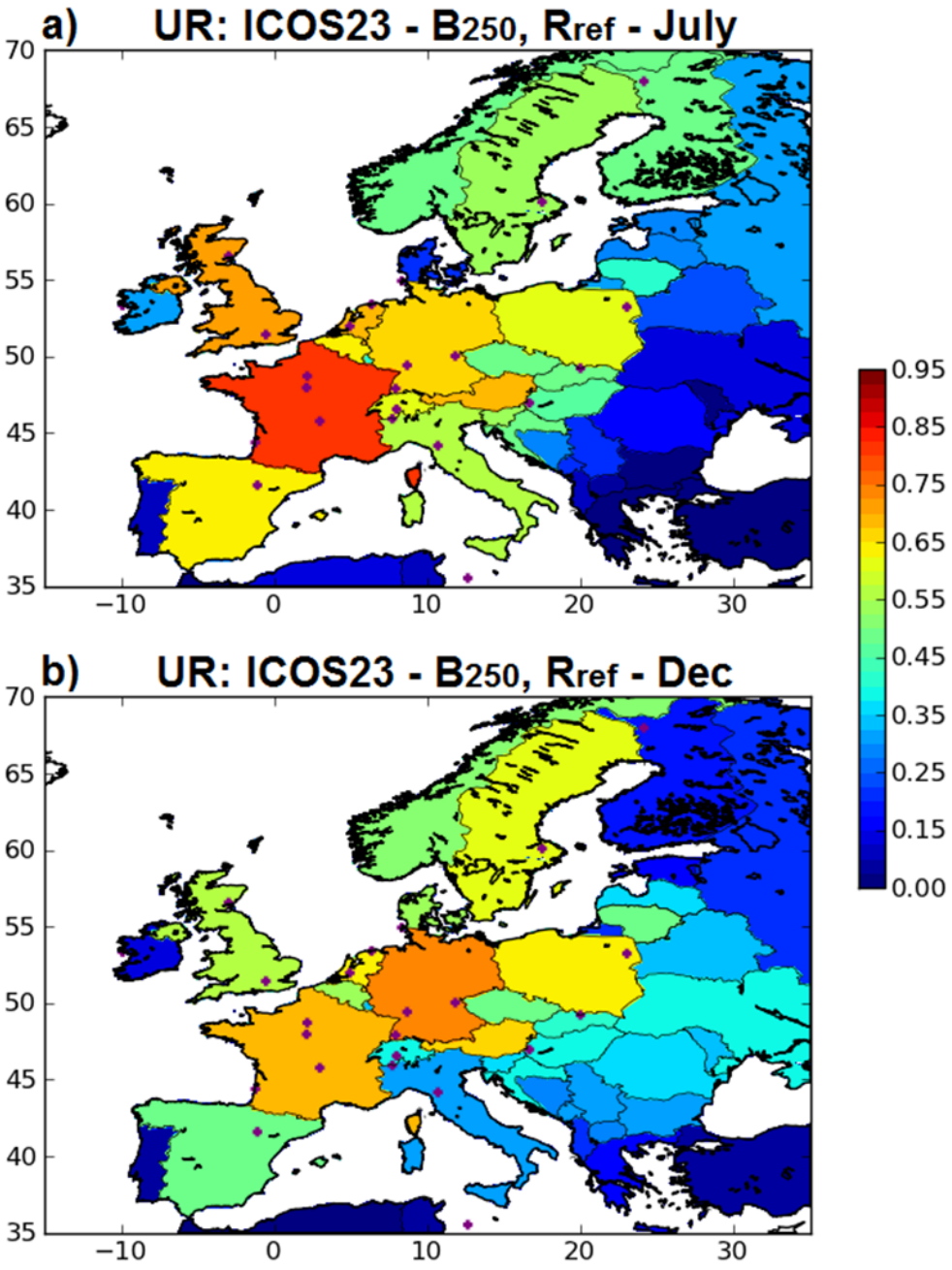

Figure 4. Uncertainty reduction (theoretically comprised between 0 and 1) for two-week mean NEE at the country scale for July **(a)** and December **(b)** when using ICOS23 and the reference

1382 inversion configuration. Red/blue colors indicate relatively high/low uncertainty reduction (with
1383 min = 0, max = 0.95 in the color scale).
1384
1385
1386
1387
1388
1389
1390
1391
1392
1393
1394
1395
1396
1397
1398
1399
1400
1401

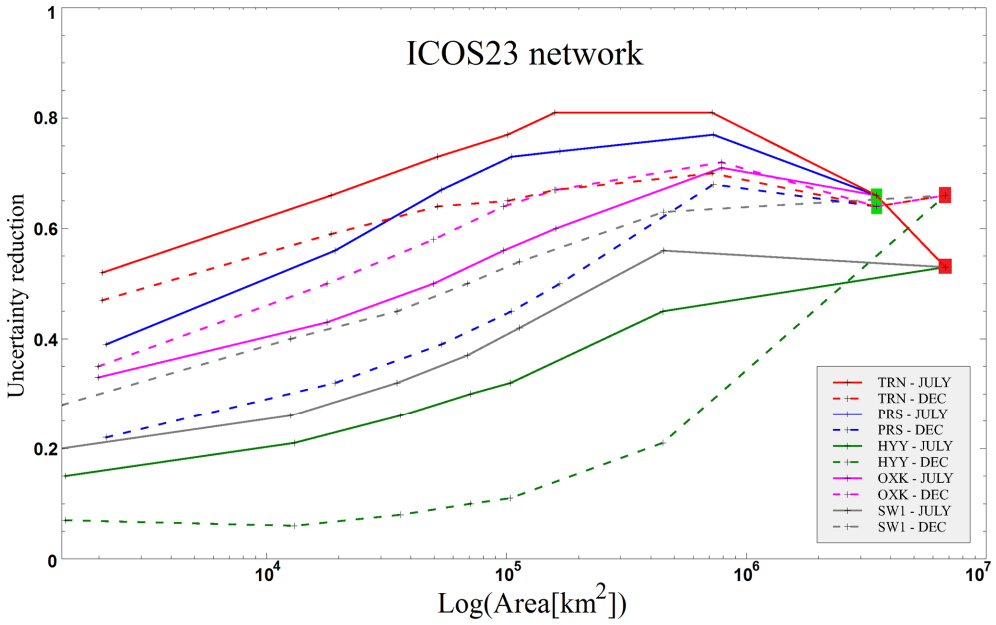

Figure 5. Uncertainty reduction (theoretically comprised between 0 and 1) for two-week mean NEE in July and December 2007 using ICOS23 and the reference configuration of the inversion, as a function of the size (logarithmic scale) of the spatial averaging area (in km^2; as indicated by the crosses, for each curve values are derived for 1.5ºx1.5º, 2.5ºx2.5º, 3.5ºx3.5º, 4.5ºx4.5º and 10.5ºx10.5º areas which correspond to different values in terms of km^2 depending on their location in Europe) around each station TRN (red curves), PRS (blue curves), HYY (green curves), OXK (pink curves) and SW1 (grey curves; see the locations in Fig. 1c). Solid and dash lines correspond to results for July and December respectively (see the legend within the figure). The results of uncertainty reduction for the whole European domain are included (red rectangles). The results for the western European domain defined in Fig. 1c are included on curves corresponding to sites which are located in this domain (TRN, PRS and OXK, see the green rectangles).

Deleted: rectangle

Deleted: rectangle

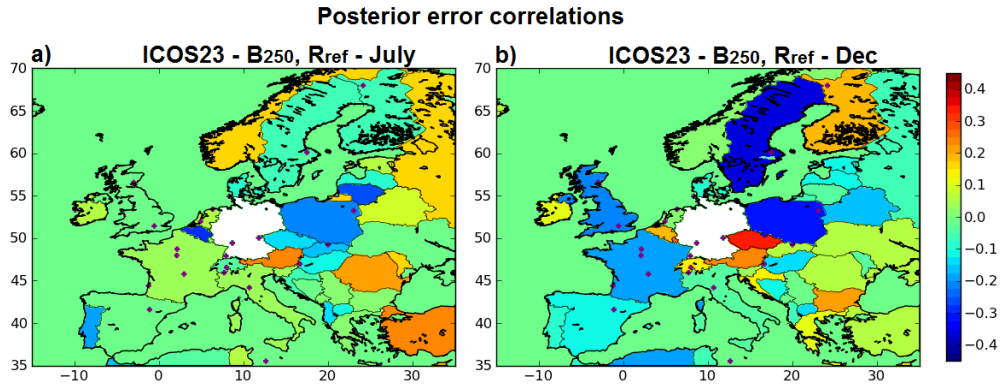

Figure 6. Correlations of the posterior uncertainties in two-week mean NEE between Germany and the other European countries in July **(a)** and December **(b)** from the reference inversions with ICOS23. Germany is masked in white. Red/blue colors indicate relatively high positive/negative correlations (with min= -0.45, max = 0.45 in the color scale).

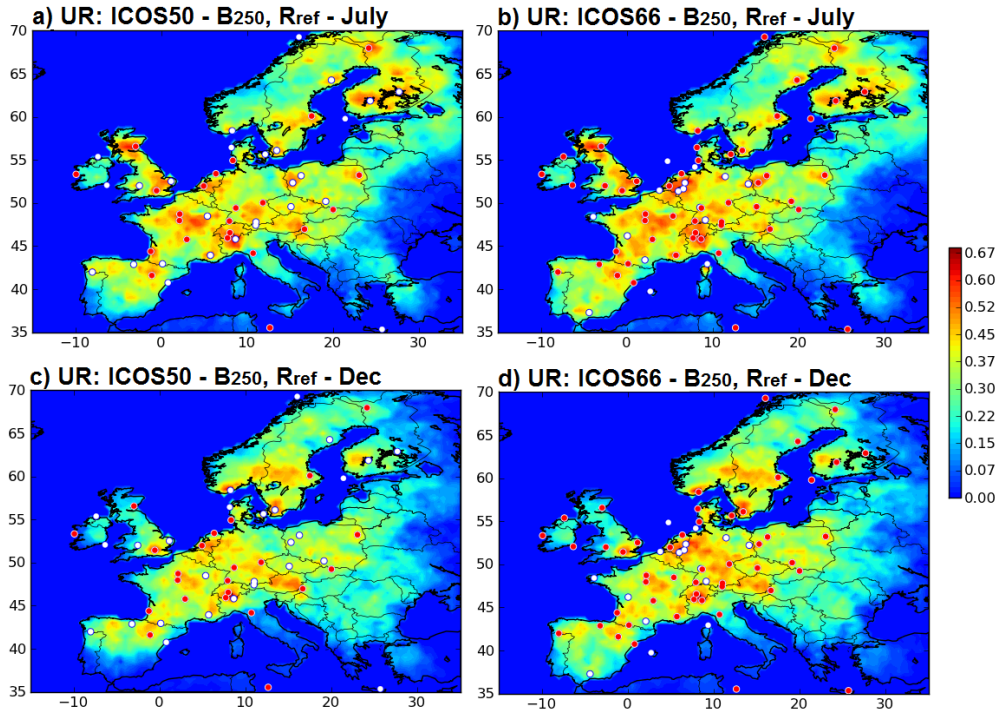

Figure 7. Uncertainty reduction (theoretically comprised between 0 and 1) for two-week mean NEE at 0.5° resolution in July **(a,b)** and December **(c,d)** when using ICOS50 **(a,c)** and ICOS66 **(b,d)** and the reference inversion configuration. Red dots corresponds to the ICOS23 **(a,c)** or ICOS50 **(b,d)** sites while white dots correspond to the additional sites included in ICOS50 or ICOS66 respectively. Red/blue colors indicate relatively high/low uncertainty reduction (with min = 0, max = 0.68 in the color scale).

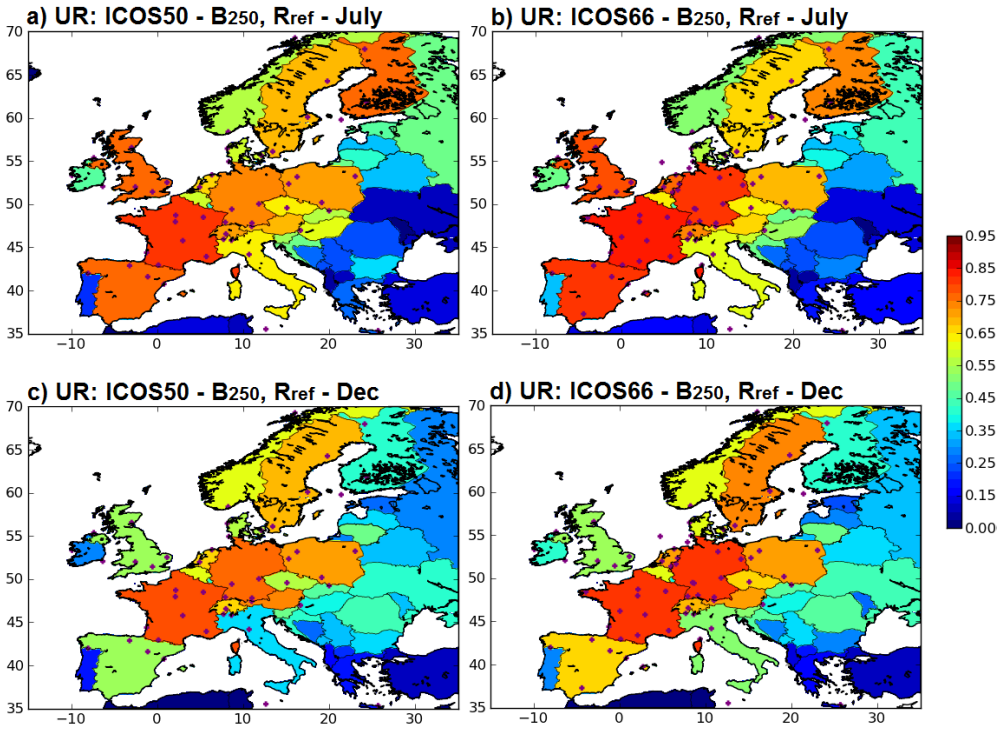

Figure 8. Uncertainty reduction (theoretically comprised between 0 and 1) for two-week mean NEE at the country scale in July **(a,b)** and December **(c,d)**, when using ICOS50 **(a,c)** and ICOS66 **(b,d)**. Red/blue colors indicate relatively high/low uncertainty reduction (with min = 0, max = 0.95 in the color scale).

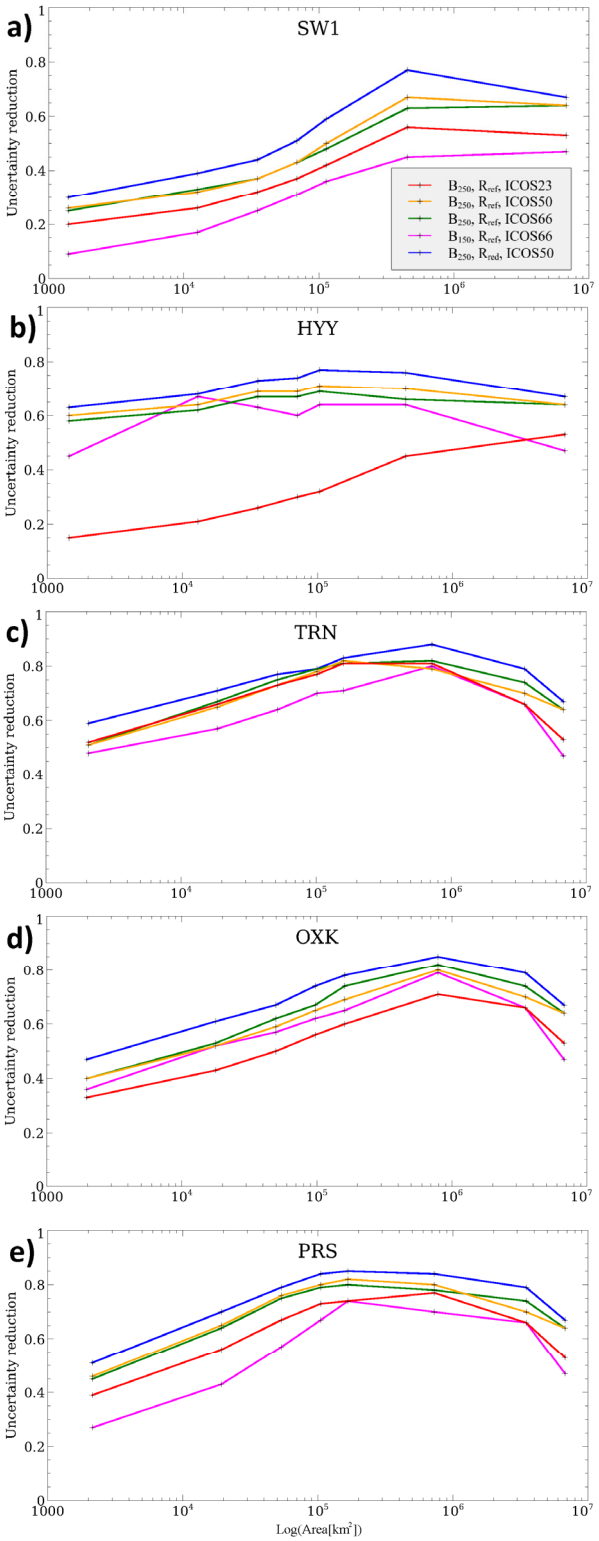
a)
SW1
b)
HYY
c)
TRN
d)
OXK
e)
PRS
Uncertainty reduction
Log(Area[km^2])
B_{250}, R_{ref}, ICOS23
B_{250}, R_{ref}, ICOS50
B_{250}, R_{ref}, ICOS66
B_{150}, R_{ref}, ICOS66
B_{250}, R_{red}, ICOS50

Figure 9. Uncertainty reduction (theoretically comprised between 0 and 1) for two-week mean NEE for July 2007 as a function of the size (in logarithmic scale) of the spatial averaging area (same as for Fig. 5) centered on **(a)** SW1, **(b)** HYY, **(c)** TRN, **(d)** OXK, and **(e)** PRS. Red, orange, green lines: results with the reference configuration of the inversion using ICOS23, ICOS50 and ICOS66 respectively; blue: results when using ICOS50 and the inversion configuration with $\mathbf{R}=\mathbf{R}_{red}$; pink: results when using ICOS66 and the inversion configuration with $\mathbf{B}=\mathbf{B}_{150}$**.** The results of uncertainty reduction for the whole European domain are included systematically. The results for the western European domain defined in Fig. 1c are included on curves corresponding to sites which are located in this domain (TRN, PRS and OXK).

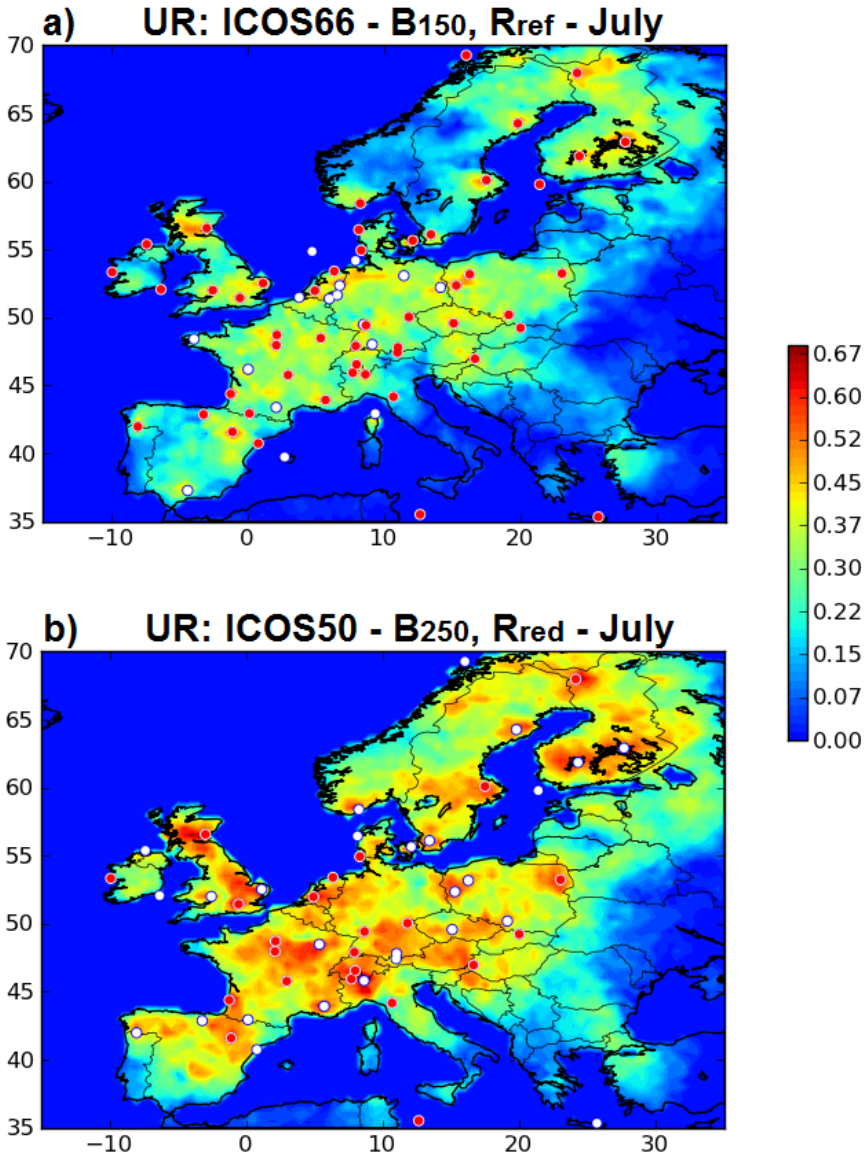

Figure 10. Uncertainty reduction (theoretically comprised between 0 and 1) for two-week mean NEE at 0.5º horizontal resolution in July when modifying the inversion configuration from the reference one: using $\mathbf{B}_{150}$ instead of $\mathbf{B}_{250}$ and ICOS66 **(a)** using $\mathbf{R}_{red}$ instead of $\mathbf{R}_{ref}$ and ICOS50 **(b)**. Red dots corresponds to the ICOS23 **(b)** or ICOS50 **(a)** sites while white dots correspond to the additional sites included in ICOS50 or ICOS66 respectively. Red/blue colors indicate relatively high/low uncertainty reduction (with min = 0, max = 0.68 in the color scale).

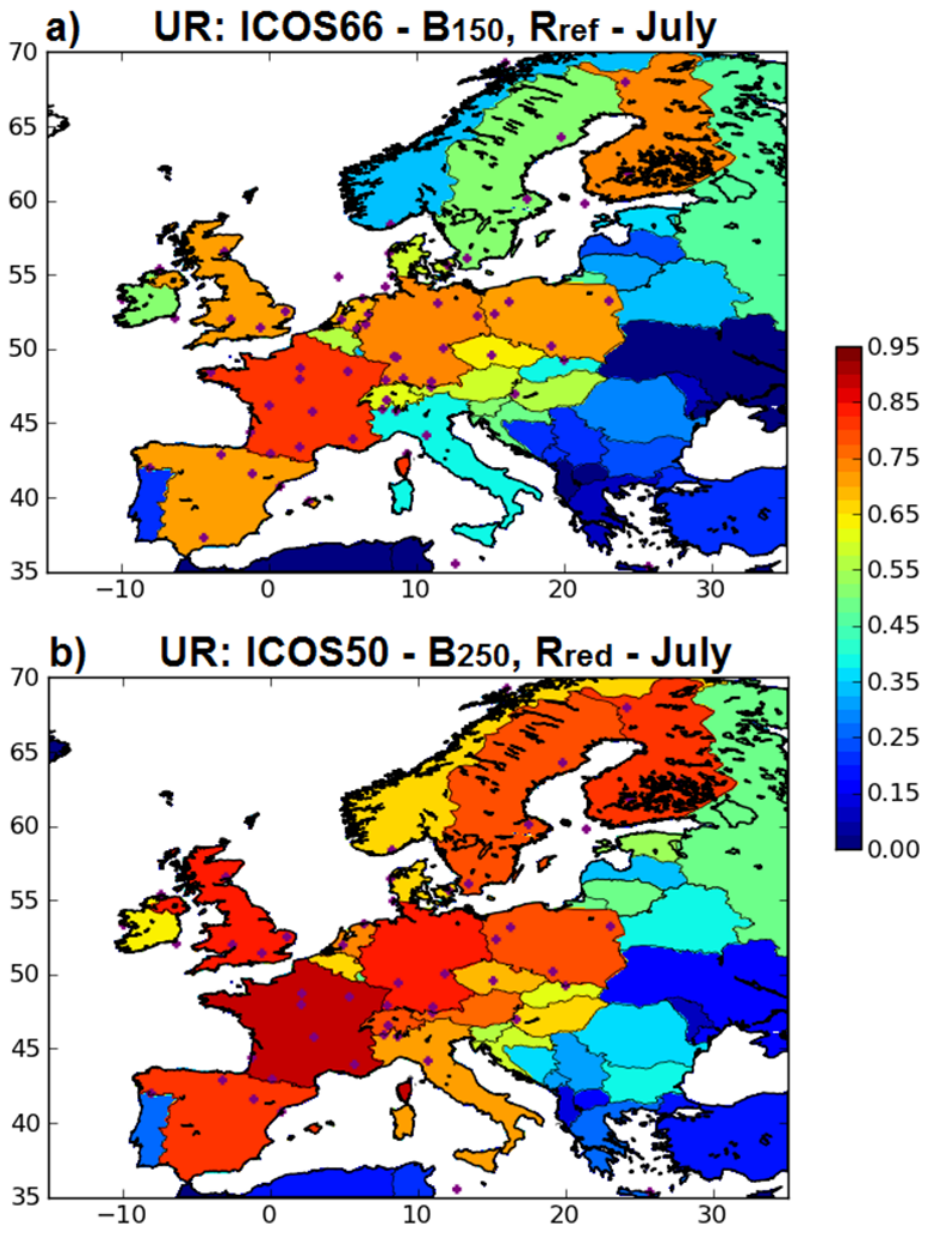

Figure 11. Uncertainty reduction (theoretically comprised between 0 and 1) for two-week mean NEE at the country scale in July when modifying the inversion configuration from the reference one by using $\mathbf{B}_{150}$ instead of $\mathbf{B}_{250}$ and ICOS66 **(a)** using $\mathbf{R}_{red}$ instead of $\mathbf{R}_{ref}$ and ICOS50 **(b)**.

Red/blue colors indicate relatively high/low uncertainty reduction (with min = 0, max = 0.95 in the color scale).

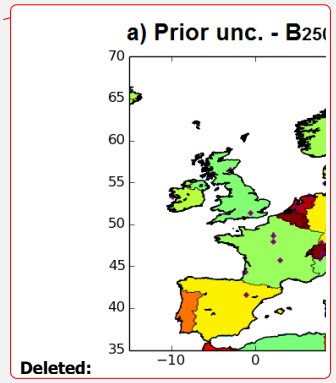

Deleted:

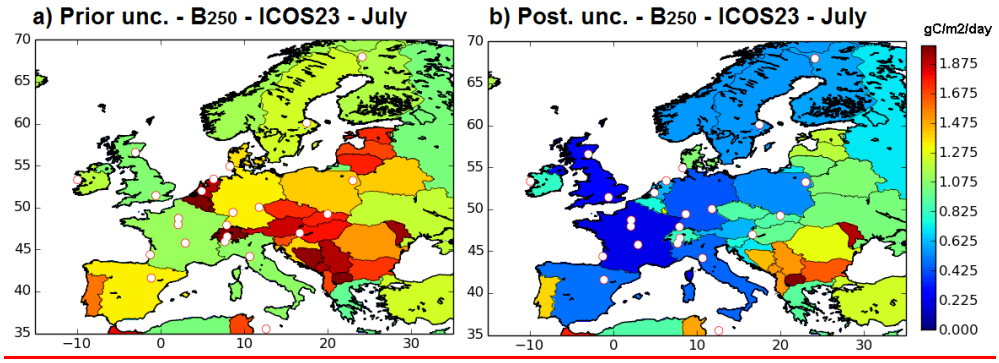

Figure 12. Standard deviations ($gCm^{-2}day^{-1}$) of the prior **(a)** and posterior **(b)** flux uncertainties at country scale. Posterior uncertainties are given for inversions using ICOS23 (white circles) and the reference inversion set-up. Red/blue colors indicate relatively high/low uncertainties (with min = 0 $gCm^{-2}day^{-1}$, max = 1.975 $gCm^{-2}day^{-1}$ in the color scale).

Deleted: red dots

Deleted: setup

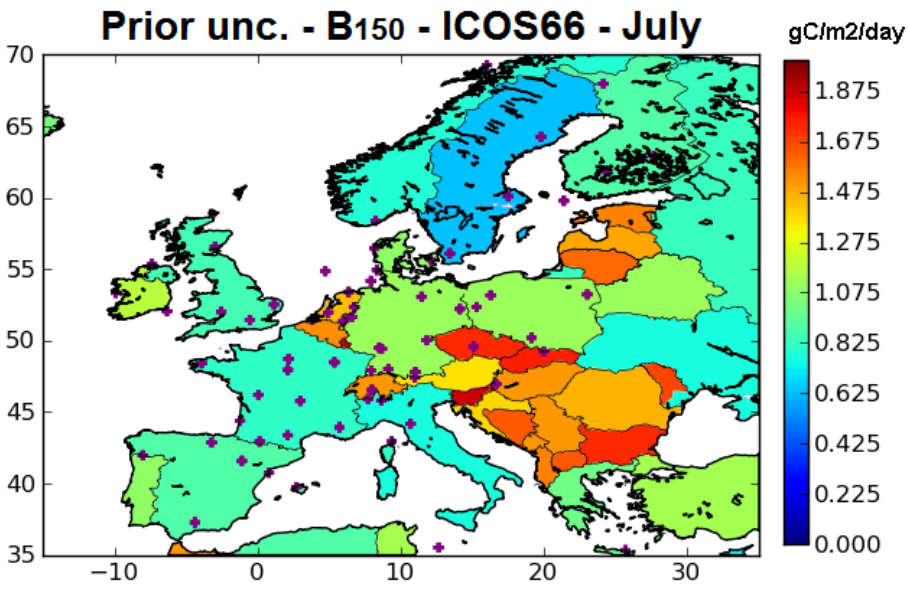

Figure A1. Standard deviations ($gCm^{-2}day^{-1}$) of the prior flux uncertainties at country scale for July when considering $\mathbf{B}_{150}$. Red dots: ICOS66. Red/blue colors indicate relatively high/low uncertainties (with min = 0 $gCm^{-2}day^{-1}$, max = 1.975 $gCm^{-2}day^{-1}$ in the color scale).

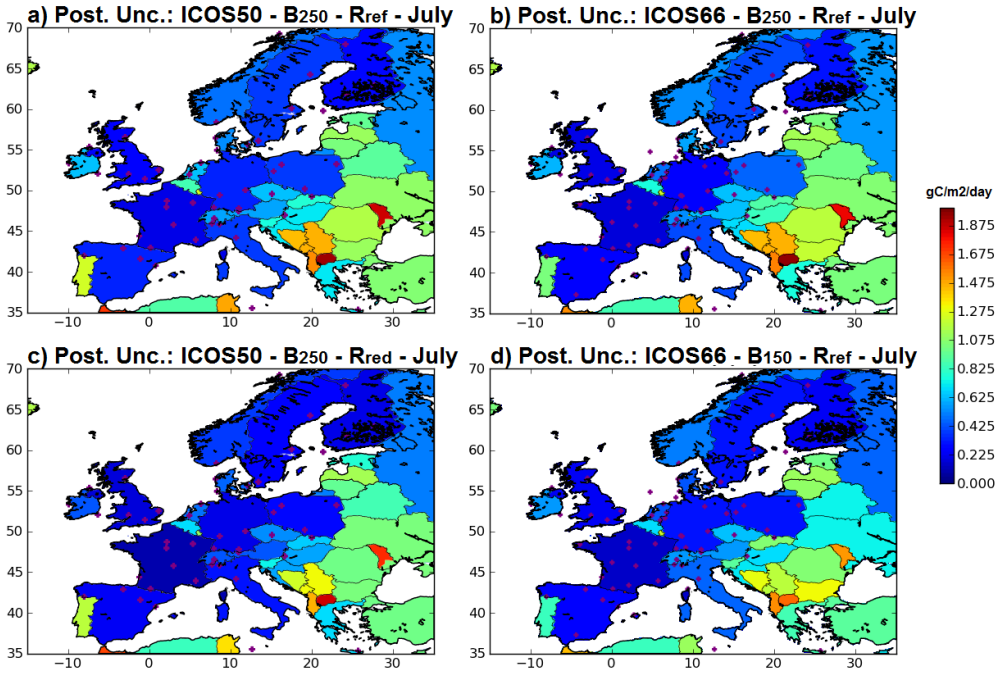

Figure A2. Standard deviations ($gCm^{-2}day^{-1}$) of the posterior uncertainties at country scale for July when using ICOS50 **(a,c)** and ICOS66 **(b,d)**, the reference inversion configuration **(a,b)**, using $\mathbf{B}_{150}$ instead of $\mathbf{B}_{250}$ **(d)** using $\mathbf{R}_{red}$ instead of $\mathbf{R}_{ref}$ **(c)**. Red/blue colors indicate relatively high/low uncertainties (with min = 0 $gCm^{-2}day^{-1}$, max = 1.975 $gCm^{-2}day^{-1}$ in the color scale).

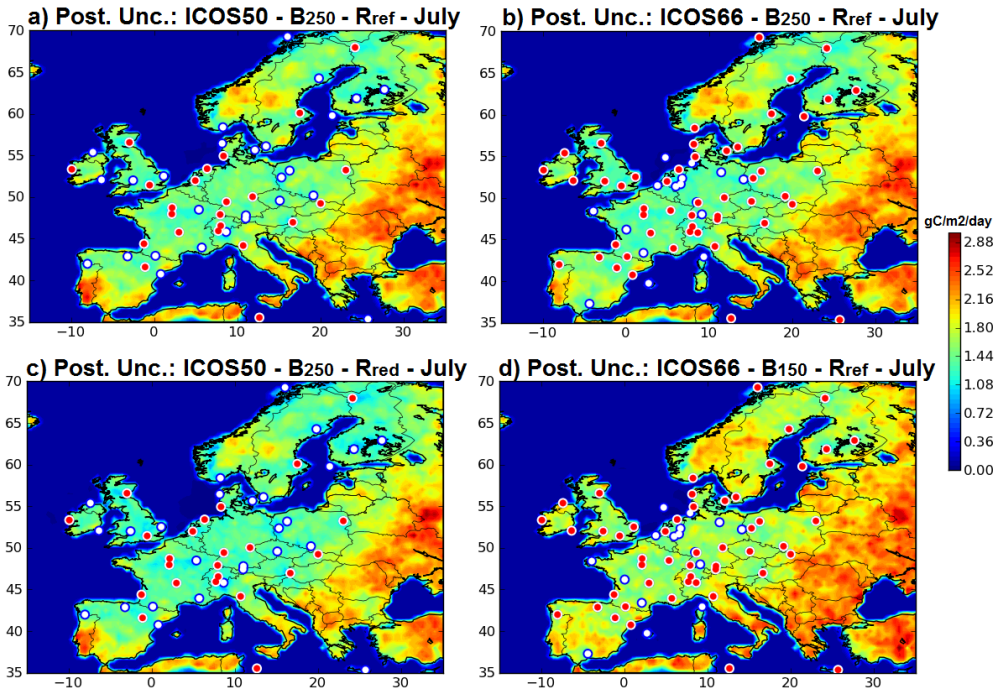

1543

1544 **Figure A3.** Standard deviations ($gCm^{-2}day^{-1}$) of the posterior uncertainties in two-week mean
1545 NEE at 0.5° resolution for July when using ICOS50 **(a,c)** and ICOS66 **(b,d)**, the reference
1546 inversion configuration **(a,b)**, using $\mathbf{B}_{150}$ instead of $\mathbf{B}_{250}$ **(d)** using $\mathbf{R}_{red}$ instead of $\mathbf{R}_{ref}$ **(c)**. Red
1547 dots corresponds to the ICOS23 **(a,c)** or ICOS50 **(b,d)** sites while white dots correspond to the
1548 additional sites included in ICOS50 or ICOS66 respectively. Red/blue colors indicate relatively
1549 high/low uncertainties (with min = 0 $gCm^{-2}day^{-1}$, max = 3 $gCm^{-2}day^{-1}$ in the color scale).